

# Stability and Robustness of a Tandem Tilt-Wing VTOL with Dynamic Inversion Control Laws

Daniel Milz\* and Marc May†

*Institute of Flight Systems, German Aerospace Center (DLR), 82234 Weßling, Germany  
TUM School of Engineering and Design, Technical University of Munich (TUM), 85521 Ottobrunn, Germany*

Sophie F. Armanini‡

*Imperial College London, London SW7 2AZ, UK*

Gertjan Looye §

*Institute of Aeroelasticity, German Aerospace Center (DLR), 82234 Weßling, Germany*

**Tilt-wing aircraft are a promising concept that combines the advantages of vertical take-off and landing (VTOL) capabilities with efficient cruise flight. However, the control design for tilt-wings poses significant challenges, particularly due to the different flight phases and the transition between them. Nonlinear dynamic inversion-based (NDI) control approaches have been demonstrated to offer an effective solution as they decouple the dynamics throughout the envelope. The susceptibility to uncertainties and disturbances arising from complex aerodynamic interactions raises questions about the stability and robustness of control systems designed for such aircraft. This study proposes methodologies for assessing the stability and robustness of control systems for transformational VTOLs. To illustrate, the stability and robustness of a hybrid NDI control system integrated within an optimization-based control allocation scheme will be examined across the different flight phases of a tandem tilt-wing VTOL. Precisely, we assess the robustness against uncertainties using worst-case disk and stability margins, as determined by the structured singular value  $\mu$ . The findings indicate that the controller can stabilize the vehicle throughout all flight phases while ensuring sufficient margins to uncertainties. However, transitioning from thrust-borne to aerodynamic flight decreases the margins as the influence of aerodynamic uncertainties increases. Additionally, the backward or decelerating transition has to be performed carefully to avoid unstable flight phases.**

## I. Introduction

TRANSFORMATIONAL or transition vertical take-off and landing (VTOL) aircraft are rising technologies in Advanced Air Mobility. They offer unparalleled flexibility in confined spaces and enable novel operational concepts by seamlessly transitioning between hover and cruise flight. Among the promising configurations are tandem tilt-wing electric VTOLs (eVTOLs), which combine the capability for vertical take-off and landings with an efficient cruise flight, all while using a single propulsion system throughout the entire envelope [1]. However, transformational VTOLs, especially tandem tilt-wings, have intricate mechanics at the tilting mechanism and exhibit complex aerodynamic characteristics, necessitating novel modeling approaches to accurately capture propeller-wing and wing-wing interactions [2, 3]. Moreover, the transition between different flight phases represents a complex and understudied phenomenon that must be addressed to enable tilt-wing operations [4]. Nevertheless, multiple endeavors have been conducted on (tandem) tilt-wing configurations, including the CL-84 [5], Airbus A<sup>3</sup> Vahana [6], NASA LA-8 [7], and other tilt-wing configurations [8–10]. Despite these efforts, controlling such aircraft, particularly during the transition phase, presents a considerable challenge due to the variations in flight dynamics.

Transformational VTOL configurations with complex aerodynamic effects and interactions create a challenging control design problem. Widespread methods for controlling these vehicles are, among others [11], especially

---

\*Research Associate, Department of Flight Control and Simulation, daniel.milz@dlr.de, AIAA member

†Research Associate, Department of Flight Control and Simulation, marc.may@dlr.de, AIAA member

‡Associate Professor, Aerial Robotics Laboratory, Department of Aeronautics, s.armanini@imperial.ac.uk, AIAA member

§Head of Department, Department of Control of Aeroelastic Systems and Flight Control Expert, Department of Flight Control and Simulation, Institute of Flight Systems, gertjan.looye@dlr.de

gain-scheduling of PID control laws [12], robust  $H_\infty$  control laws [13], or optimal LQR control laws [14–16]. The commonality of these linear methods is that they are only partly suitable for these dynamics and inherently require scheduling techniques to ensure satisfactory performance over the different flight regimes. This increases the design effort since the synthesis must be performed for multiple flight conditions. Alternative approaches employ adaptive control techniques [17, 18] and nonlinear dynamic inversion (NDI)-based control laws [8, 19–24]. The latter is the most popular method currently applied as it provides an inherent solution to the aforementioned requirements while simultaneously providing physical interpretation, (global) decoupling of the dynamics, and a modular and reusable flight controller design [22].

In previous publications [25–27], we proposed a generalized nonlinear control approach for VTOLs and demonstrated its efficacy on a tandem tilt-wing under nominal conditions. A hybrid NDI angular rate and velocity inversion is integrated with an optimization-based control allocation scheme cascaded with a parallel attitude and flight path controller. The integration of translational and rotational loops enables multi-phase flight and transition maneuvers that utilize all available degrees of freedom while allocating control effectors optimally. Hybrid NDI [28–30] control design approach is a promising method for flight control, as it provides a trade-off between model-based and sensory NDI. While increasing the robustness to model uncertainties, it also dampens the aggressiveness of sensory NDI methods and provides an intuitive control allocation task. This allows for complete envelope control of the transformational VTOL.

However, these works lack investigations of the stability and robustness of the closed-loop system. Disk margins provide a rigorous framework for quantifying robust stability margins against simultaneous gain and phase variations in feedback control systems, both at the input and output. Unlike classical gain and phase margins, which evaluate robustness to perturbations independently, disk margins characterize the largest region of complex uncertainty that preserves closed-loop stability [31]. The structured singular value  $\mu$  quantifies the stability margin in the presence of structured uncertainties. Both methods give a guaranteed worst-case boundary for the influence of uncertainties on the performance and robustness. Similar work has been done in [32, 33].

To attain confidence for flight tests, ensure flight safety, and initiate flight control law clearance, it is crucial to rigorously investigate the stability and robustness of the closed-loop system. Establishing acceptable criteria and a clear framework poses a complex task for VTOL systems, as it is challenging to rigorously prove their stability. Thus, we propose initial means of compliance to define a framework with acceptable criteria that indicate stability. This work contributes linear stability and robustness analysis of the tandem tilt-wing eVTOL along nominal trajectories or in a static flight envelope. We follow the subsequent approach:

- 1) Model definition for control design and analysis (cf. Section II)
  - a) Discussions on the considered physical effects and assumptions made (cf. [34, 35])
  - b) Definition of a mathematical model and validation against experimental data (ongoing, cf. [35, 36])
  - c) Linear analysis of the open-loop system to understand the control challenges (cf. Section V)
- 2) Appropriate control design (cf. Section III)
  - a) Discussion of the stability under the selected dynamic inversion control strategy (cf. Section III)
  - b) Controllability analysis throughout the envelope for the control allocation (cf. Section III)
- 3) Stability and performance through nonlinear simulations in nominal conditions (cf. [27])
- 4) Closed-loop stability margin and robustness using worst-case disk and stability margins throughout the envelope using trajectories from [4]. The linearized process and analysis metrics are described in Section IV. Section VI contains the results of the closed-loop analysis.

The study is concluded in Section VII.

## II. Flight Dynamics Model

Fig. 1 shows a sketch of the tandem tilt-wing model with inputs annotated. The configuration distinguishes itself from other tilt-wing or eVTOL configurations by featuring eight electrically driven propellers and two independent tandem tilt-wings. The wings have vertical and horizontal displacement in order to minimize possible interactions. Furthermore, each half-wing is equipped with one elevon, which combines aileron and elevator functionalities. Finally, the propeller rotation directions are chosen to enable a complete moment cancellation in nominal flight and to facilitate yaw maneuvers during hover flight using differential propeller torques. The wings have a *NASA GA(W)-2* airfoil. A further description of the flight dynamics model is given in [34, 35, 37, 38].

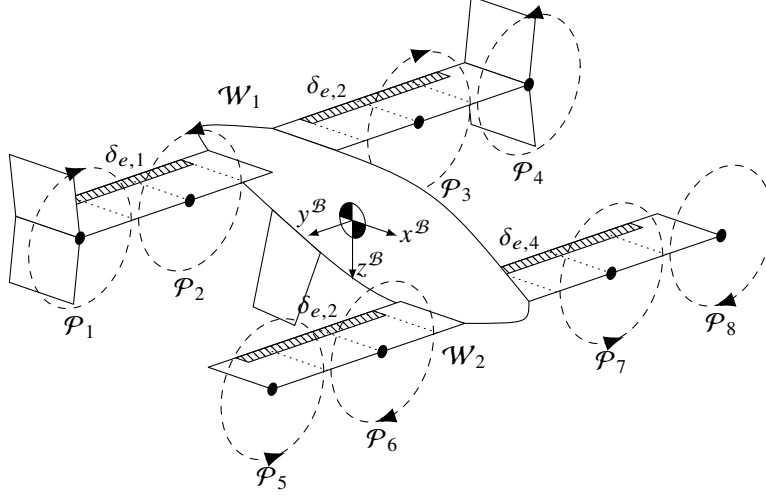


Fig. 1 3D sketch of the tandem tilt-wing configuration.

### A. Equations of Motion

Let  $\mathcal{N}$  denote the north-east-down (NED) earth frame as an inertial frame,  $\mathcal{B}$  the body frame,  $\mathcal{W}_i$  the wing frames, and  $\mathcal{P}_i$  the propeller frames. The rotation between the frames is described by the rotation matrix  $\mathbf{R}_B^A = \mathbf{R}_{A \leftarrow B}$ .

Let the state vector  $x$  be represented by the aircraft position in NED frame  $\mathbf{r}_B^{\mathcal{N}}$ , the rotation matrix  $\mathbf{R}_B^{\mathcal{N}}$  or the Euler angles  $\Theta$ , the aircraft velocity in body frame  $\mathbf{v}^{\mathcal{B}}$ , and the angular rates in the body frame  $\omega^{\mathcal{B}}$ . Furthermore, let  $\mathbf{R}_B^{\Theta}$  denote the transformation matrix from body angular velocities to the Euler angle rates, and  $m$  the total mass. The moment of inertia  $\mathbf{J}_{\text{cg}}^{\mathcal{B}}$  and the aircraft's center of gravity  $\mathbf{r}_{\text{cg}}^{\mathcal{B}}$  depend on the current wing configuration, i.e., the tilt angles  $\delta_{w,1}$  and  $\delta_{w,2}$ .  $\mathbf{f}^{\mathcal{B}}$  and  $\mathbf{m}^{\mathcal{B}}$  represent the forces and moments in the body frame, with considerable contributions from aerodynamics, including the propeller slipstream, and the propulsion system, including propeller inflow and gyroscopic effects. The nonlinear state-space representation using first-order differential equations of the tandem tilt-wing eVTOL can be described by

$$\dot{\mathbf{r}}^{\mathcal{N}} = \mathbf{R}_B^{\mathcal{N}}(\Theta) \mathbf{v}^{\mathcal{B}} \quad (1a)$$

$$\dot{\Theta} = \mathbf{R}_B^{\Theta}(\Theta) \omega^{\mathcal{B}} \quad (1b)$$

$$\dot{\mathbf{v}}^{\mathcal{B}} = \mathbf{R}_B^{\mathcal{N}}(\Theta)^T \mathbf{g}^{\mathcal{N}} - \omega^{\mathcal{B}} \times \mathbf{v}^{\mathcal{B}} + \frac{1}{m} \mathbf{f}^{\mathcal{B}}(x, u) \quad (1c)$$

$$\dot{\omega}^{\mathcal{B}} = \mathbf{J}_{\text{cg}}^{\mathcal{B}-1} \left( -\omega^{\mathcal{B}} \times \mathbf{J}_{\text{cg}}^{\mathcal{B}} \omega^{\mathcal{B}} \right) + \mathbf{J}_{\text{cg}}^{\mathcal{B}-1} \mathbf{m}^{\mathcal{B}}(x, u) \quad (1d)$$

with the state vector  $x = [\mathbf{r}^{\mathcal{N}}, \Theta, \mathbf{v}^{\mathcal{B}}, \omega^{\mathcal{B}}]^T$  and the input vector  $u = [\delta_{w,1 \dots 2}, n_{1 \dots 8}, \delta_{e,1 \dots 4}]^T$  consisting of the propeller speeds  $n_i$  in  $\text{s}^{-1}$ , the tilt-wing angles  $\delta_{w,i}$ , and the elevon control surface deflections  $\delta_{e,i}$ , and the gravitational acceleration vector  $\mathbf{g}^{\mathcal{N}} = [0, 0, 9.81 \text{ m s}^{-2}]^T$ . As the operating altitude for the configuration is generally low, changes in the air density  $\rho$  are negligible and a constant value of  $\rho = 1.225 \text{ kg m}^{-3}$  is assumed.

### B. Weight and Balance

The aircraft's center of gravity  $\mathbf{r}_{\text{cg}}^{\mathcal{B}}$  and its inertia tensor  $\mathbf{J}_{\text{cg}}^{\mathcal{B}}$  shift when the wings tilt because of the wing mass distribution. This effect can be modeled by the parallel-axis theorem applied the three rigid bodies with fixed centers of mass (CM), i.e., fuselage (mass  $m_f$ , CM position  $\mathbf{r}_{f,\text{cm}}^{\mathcal{B}}$ , inertia  $\mathbf{J}_{f,\text{cm}}^{\mathcal{B}}$ ), main wing (mass  $m_{w1}$ , CM position  $\mathbf{r}_{w1,\text{cm}}^{\mathcal{W}_1}$ , inertia  $\mathbf{J}_{w1,\text{cm}}^{\mathcal{W}_1}$ ), and canard wing (mass  $m_{w2}$ , CM position  $\mathbf{r}_{w2,\text{cm}}^{\mathcal{W}_2}$ , inertia  $\mathbf{J}_{w2,\text{cm}}^{\mathcal{W}_2}$ ). The total mass is  $m = m_f + m_{w1} + m_{w2}$ . The wings rotate around the y-axis at the hinge points  $\mathbf{r}_{w1}^{\mathcal{B}}$  and  $\mathbf{r}_{w2}^{\mathcal{B}}$ . Then, the total center of gravity can be calculated as

$$\mathbf{r}_{\text{cg}}^{\mathcal{B}} = \underbrace{\frac{m_f}{m} \mathbf{r}_{f,\text{cm}}^{\mathcal{B}} + \frac{m_{w1}}{m} \mathbf{r}_{w1}^{\mathcal{B}} + \frac{m_{w2}}{m} \mathbf{r}_{w2}^{\mathcal{B}}}_{\text{const.}} + \underbrace{\frac{m_{w1}}{m} \mathbf{R}_{\mathcal{W}_1}^{\mathcal{B}} \mathbf{r}_{w1,\text{cm}}^{\mathcal{W}_1}}_{\text{of } \delta_{w1}} + \underbrace{\frac{m_{w2}}{m} \mathbf{R}_{\mathcal{W}_2}^{\mathcal{B}} \mathbf{r}_{w2,\text{cm}}^{\mathcal{W}_2}}_{\text{of } \delta_{w2}} \quad (2)$$

and the total moment of inertia as

$$\begin{aligned} \mathbf{J}_{\text{cg}}^{\mathcal{B}} &= \mathbf{J}_{\text{f,cm}}^{\mathcal{B}} + \mathbf{R}_{\mathcal{W}_1}^{\mathcal{B}} \mathbf{J}_{\mathcal{W}_1,\text{cm}}^{\mathcal{W}_1} \mathbf{R}_{\mathcal{B}}^{\mathcal{W}_1} + \mathbf{R}_{\mathcal{W}_2}^{\mathcal{B}} \mathbf{J}_{\mathcal{W}_2,\text{cm}}^{\mathcal{W}_2} \mathbf{R}_{\mathcal{B}}^{\mathcal{W}_2} \\ &\quad - m_f \left[ \mathbf{r}_{\text{cg}}^{\mathcal{B}} - \mathbf{r}_{\text{f,cm}}^{\mathcal{B}} \right]_{\times}^2 - m_{\mathcal{W}_1} \left[ \mathbf{r}_{\text{cg}}^{\mathcal{B}} - \mathbf{r}_{\mathcal{W}_1}^{\mathcal{B}} - \mathbf{R}_{\mathcal{W}_1}^{\mathcal{B}} \mathbf{r}_{\mathcal{W}_1,\text{cm}}^{\mathcal{W}_1} \right]_{\times}^2 - m_{\mathcal{W}_2} \left[ \mathbf{r}_{\text{cg}}^{\mathcal{B}} - \mathbf{r}_{\mathcal{W}_2}^{\mathcal{B}} - \mathbf{R}_{\mathcal{W}_2}^{\mathcal{B}} \mathbf{r}_{\mathcal{W}_2,\text{cm}}^{\mathcal{W}_2} \right]_{\times}^2 \end{aligned} \quad (3)$$

with the cross product skew symmetric matrix  $[\cdot]_{\times}$ . As the position of the center of gravity also depends on the current tilt angles, there is no beneficial reduction of the formula possible. The values of the parameters for the weight and balance are shown in the Appendix in Table 4.

### C. Propulsive Forces and Moments

The propeller  $p$  mainly introduces thrust and its rotational torque into the system. However, in the case of non-axial inflow, the propeller also exhibits lateral forces and moments, and reduces its efficiency. The forces and moments can be approximated by coefficients depending on the propellers advance ratio for each axis in the local propeller frame  $\mathcal{P}_p$ :

$$\lambda_{p,x} = \frac{v_x^{\mathcal{P}_p}}{n_p R}, \quad \lambda_{p,y} = \frac{v_y^{\mathcal{P}_p}}{n_p R}, \quad \lambda_{p,z} = \frac{v_z^{\mathcal{P}_p}}{n_p R} \quad (4)$$

depending on the the propeller radius  $R = 0.75$  m and its rotational velocity  $n_p$  in  $\text{s}^{-1}$ . The forces and moments are:

$$\mathbf{f}_{p,p}^{\mathcal{P}_p} = \frac{\rho \pi R^4}{2} \left[ (c_{T_0} - c_{T_\lambda} \lambda_x), \quad c_{H_\lambda} \lambda_y, \quad c_{H_\lambda} \lambda_z \right]^T n_p^2 \quad (5a)$$

$$\mathbf{m}_{p,p}^{\mathcal{P}_p} = -\text{sgn } n_i \frac{\rho \pi R^5}{2} \left[ (c_{Q_0} - c_{Q_\lambda} \lambda_x), \quad c_{P_\lambda} \lambda_y, \quad c_{P_\lambda} \lambda_z \right]^T n_p^2 \quad (5b)$$

with the coefficients shown in Table 5 and defined in [38]. This model can be simplified by canceling out the advance ratios that possibly cause singularities to

$$\mathbf{f}_{p,p}^{\mathcal{P}_p} = \frac{\rho \pi R^4}{2} \begin{bmatrix} c_{T_0} \\ 0 \\ 0 \end{bmatrix} n_p^2 - \frac{\rho \pi R^3}{2} \begin{bmatrix} c_{T_\lambda} & 0 & 0 \\ 0 & c_{H_\lambda} & 0 \\ 0 & 0 & c_{H_\lambda} \end{bmatrix} \mathbf{v}^{\mathcal{P}_p} |n_p| \quad (5c)$$

$$\mathbf{m}_{p,p}^{\mathcal{P}_p} = -\text{sgn } n_p \frac{\rho \pi R^5}{2} \begin{bmatrix} c_{Q_0} \\ 0 \\ 0 \end{bmatrix} n_p^2 - \frac{\rho \pi R^4}{2} \begin{bmatrix} c_{Q_\lambda} & 0 & 0 \\ 0 & c_{P_\lambda} & 0 \\ 0 & 0 & c_{P_\lambda} \end{bmatrix} \mathbf{v}^{\mathcal{P}_p} n_p \quad (5d)$$

where the first part represents the nominal propeller model and the second part the effects due to inflow described by the inflow vector

$$\mathbf{v}^{\mathcal{P}_p} = \mathbf{R}_{\mathcal{B}}^{\mathcal{P}_p} \left( \mathbf{v}^{\mathcal{B}} + \boldsymbol{\omega}^{\mathcal{B}} \times \mathbf{r}_{p,p}^{\mathcal{B}} \right) \quad (6)$$

The axial thrust used in Section II.D is defined as  $T_p = \mathbf{f}_{p,p,x}^{\mathcal{B}}$ .

**Gyroscopic moments** are torques that must be applied to change the direction of an angular momentum vector due to the conservation of angular momentum. The angular momentum of the  $p$ -th propeller in the inertial frame  $\mathbf{L}_{p,p}^{\mathcal{N}}$  is described by

$$\mathbf{L}_{p,p}^{\mathcal{N}} = \mathbf{J}_{p,p}^{\mathcal{N}} \boldsymbol{\omega}_{p,p}^{\mathcal{N}} = \mathbf{R}_{\mathcal{B}}^{\mathcal{N}} \mathbf{R}_{\mathcal{P}_p}^{\mathcal{B}} \mathbf{J}_{p,p}^{\mathcal{P}_p} \boldsymbol{\omega}_{p,p}^{\mathcal{P}_p} \quad (7)$$

The conservation of angular momentum states that a moment  $\mathbf{m}_{\text{dL}}^{\mathcal{N}}$  is required to change an angular momentum (magnitude and direction) and holds w.r.t. the inertial frame, i.e.,

$$\mathbf{m}_{\text{dL}}^{\mathcal{N}} = \frac{d}{dt} \mathbf{L}^{\mathcal{N}} = \left( [\boldsymbol{\omega}_{\mathcal{B}}^{\mathcal{N}}]_{\times} \mathbf{R}_{\mathcal{B}}^{\mathcal{N}} \mathbf{R}_{\mathcal{P}_p}^{\mathcal{B}} + \mathbf{R}_{\mathcal{B}}^{\mathcal{N}} [\boldsymbol{\omega}_{\mathcal{P}_p}^{\mathcal{B}}]_{\times} \mathbf{R}_{\mathcal{P}_p}^{\mathcal{B}} \right) \mathbf{J}_{p,p}^{\mathcal{P}_p} \boldsymbol{\omega}_{p,p}^{\mathcal{P}_p} + \mathbf{R}_{\mathcal{B}}^{\mathcal{N}} \mathbf{R}_{\mathcal{P}_p}^{\mathcal{B}} \mathbf{J}_{p,p}^{\mathcal{P}_p} \dot{\boldsymbol{\omega}}_{p,p}^{\mathcal{P}_p} \quad (8a)$$

when assuming constant moment of inertia of the propeller, i.e.,  $\dot{\mathbf{J}}_{p,p}^{\mathcal{P}} = 0$ . Using the aircraft configuration, several symmetries can be exploited, leading to the gyroscopic moment in the body frame

$$\mathbf{m}_{dL}^{\mathcal{B}} = \mathbf{R}_{\mathcal{B}}^{\mathcal{N}} \mathbf{m}_{dL}^{\mathcal{N}} = \left[ \boldsymbol{\omega}_{\mathcal{B}}^{\mathcal{B}} + \boldsymbol{\omega}_{\mathcal{P}_p}^{\mathcal{B}} \right]_{\times} \mathbf{R}_{\mathcal{P}_p}^{\mathcal{B}} \mathbf{J}_{p,p}^{\mathcal{P}} \boldsymbol{\omega}_{p,p}^{\mathcal{P}} + \mathbf{R}_{\mathcal{P}_p}^{\mathcal{B}} \mathbf{J}_{p,p}^{\mathcal{P}} \dot{\boldsymbol{\omega}}_{p,p}^{\mathcal{P}} \quad (8b)$$

$$= \begin{bmatrix} -\sin \delta_{w,p} \left( \omega_y^{\mathcal{B}} + \dot{\delta}_{w,p} \right) \\ \omega_x^{\mathcal{B}} \sin \delta_{w,p} + \omega_z^{\mathcal{B}} \cos \delta_{w,p} \\ -\cos \delta_{w,p} \left( \omega_y^{\mathcal{B}} + \dot{\delta}_{w,p} \right) \end{bmatrix} \mathbf{J}_{xx,p,p}^{\mathcal{P}} 2\pi n_p + \begin{bmatrix} \cos \delta_{w,p} \\ 0 \\ -\sin \delta_{w,p} \end{bmatrix} \mathbf{J}_{xx,p,p}^{\mathcal{P}} 2\pi \dot{n}_p \quad (8c)$$

where  $\delta_{w,p}$  is the wing corresponding to propeller  $p$  and assuming that the propeller rotates solely around its main axis. The inertia of the propeller is assumed to be  $\mathbf{J}_{xx,p,p}^{\mathcal{P}} = 0.45 \text{ kg m}^2$ .

**Slipstream and Swirl Velocity** The induced velocity or axial slipstream velocity can then be approximated as

$$\mathbf{v}_{ax,j}^{\mathcal{W}} = \frac{s_{sc}}{2} \left( -\mathbf{v}_{N,j}^{\mathcal{W}} + \sqrt{\left( \mathbf{v}_{N,j}^{\mathcal{W}} \right)^2 + \frac{2T_j}{\rho\pi R^2}} \right) \quad (9)$$

with the mean slipstream contraction factor  $s_{sc} \approx 1$  [37] the thrust  $T_j$  acting on the segment  $j$ . The swirl induces an additional tangential velocity on the wing segments behind the propeller and can be approximated as derived in [37] as

$$\mathbf{v}_{t,j}^{\mathcal{W}} = \pm c_{vt} \sqrt{T_j} \quad (10)$$

with the swirl factor  $c_{vt} \approx 0.03$  [37] and the direction depending on the propeller rotation direction as shown in Fig. 1.

#### D. Aerodynamic Forces and Moments

The aerodynamic effects are approximated through a strip theory approach as described in detail in [35]. The main effect is assumed to be the propeller slipstream induced axial velocity in the wing frame  $\mathbf{v}_{ax,p}^{\mathcal{W}}$ , which adds up to the free flow velocity in the wing frame  $\mathbf{v}_{N,p}^{\mathcal{W}}$  for the wing segment  $j$ :

$$\mathbf{v}_{N,j}^{\mathcal{W}} = \mathbf{R}_{\mathcal{B}}^{\mathcal{W}} \left( \mathbf{v}^{\mathcal{B}} + \boldsymbol{\omega}^{\mathcal{B}} \times \mathbf{r}_{p,j}^{\mathcal{B}} \right) \quad (11)$$

with the position of the propeller  $\mathbf{r}_{p,j}^{\mathcal{B}}$ . The total velocity vector on each wing segment in the wing frame is then given as

$$\mathbf{v}_j^{\mathcal{W}} = \mathbf{v}_{N,j}^{\mathcal{W}} + \begin{bmatrix} \mathbf{v}_{ax,j}^{\mathcal{W}} & 0 & \mathbf{v}_{t,j}^{\mathcal{W}} \end{bmatrix}^T \quad (12)$$

where the mapping between the propellers and wing segments is in such a way that the four outer wing segments are completely wetted by the outer propellers, and the inner segments each by one half the propeller.

The aerodynamic forces and moments can be stated by using aerodynamic coefficient functions for the lift force  $C_L$ , side force  $C_Y$ , drag force  $C_D$ , and the pitch moment  $C_m$  as described in [37]. The three dimensional distribution of those induces the roll and yaw moments of the overall aircraft. Each segment  $j$  generates a lift and drag force as well as a pitch moment. The main contributions to the side force are the fuselage, the legs, and the wingtips. Furthermore, the fuselage exhibits a lift and drag force, too, which only depend on the free flow. However, for simplicity it is assumed to only depend on the free flow.

The total aerodynamic forces  $\mathbf{f}_a^{\mathcal{B}}$  and moments  $\mathbf{m}_a^{\mathcal{B}}$  resolved in the body frame are approximated by the aerodynamic effects, forces and moments of the body and the wing segments  $1 \leq j \leq 12$

$$\mathbf{f}_a^{\mathcal{B}} = \sum_j \frac{1}{2} \rho \left\| \mathbf{v}_j^{\mathcal{W}} \right\|_2^2 \underbrace{\mathbf{R}_y \left( \alpha_j^{\mathcal{W}} - \delta_{w,j} \right) \begin{bmatrix} -C_D^{\mathcal{W}} \left( \alpha_j^{\mathcal{W}}, \delta_{e,j} \right) & 0 & -C_L^{\mathcal{W}} \left( \alpha_j^{\mathcal{W}}, \delta_{e,j} \right) \end{bmatrix}^T}_{\mathbf{f}_j^{\mathcal{B}}} \quad (13a)$$

$$\mathbf{m}_a^{\mathcal{B}} = \sum_j \frac{1}{2} \rho \left\| \mathbf{v}_j^{\mathcal{W}} \right\|_2^2 \mathbf{R}_y \left( \alpha_j^{\mathcal{W}} - \delta_{w,j} \right) \begin{bmatrix} 0 & C_m^{\mathcal{W}} \left( \alpha_j^{\mathcal{W}}, \delta_{e,j} \right) & 0 \end{bmatrix}^T + \mathbf{r}_j^{\mathcal{B}} \times \mathbf{f}_j^{\mathcal{B}} \quad (13b)$$

with the rotation matrix around the y-axis  $\mathbf{R}_y$ , the wing segment position in the body frame  $\mathbf{r}_j^{\mathcal{B}}$  and the angle of attack  $\alpha$  being calculated from the corresponding velocity vector as

$$\alpha_j^{\mathcal{W}} = \arctan \frac{\mathbf{v}_{j,z}^{\mathcal{W}}}{\mathbf{v}_{j,x}^{\mathcal{W}}} \quad (14)$$

The aerodynamic forces and moments introduced by the fuselage can be approximated using the freeflow aerodynamic quantities in the body frame, i.e., the velocity  $\mathbf{v}^{\mathcal{B}}$ , the angle of attack  $\alpha^{\mathcal{B}}$ , and the angle of sideslip  $\beta^{\mathcal{B}}$ , leading to

$$\mathbf{f}_f^{\mathcal{B}} = \frac{\rho}{2} \|\mathbf{v}^{\mathcal{B}}\|_2^2 \begin{bmatrix} -C_D^{\mathcal{B}}(\alpha^{\mathcal{B}}) & C_Y^{\mathcal{B}}(\beta^{\mathcal{B}}) & -C_L^{\mathcal{B}}(\alpha^{\mathcal{B}}) \end{bmatrix}^T \quad (15a)$$

$$\mathbf{m}_f^{\mathcal{B}} = \frac{\rho}{2} \|\mathbf{v}^{\mathcal{B}}\|_2^2 \begin{bmatrix} 0 & 0 & 0 \end{bmatrix}^T \quad (15b)$$

where the coefficients are approximated according to [37].

The wing tips and the *inverted V* structure increase lateral stability by introducing mainly lateral moments and forces. Both have a symmetric NACA-0009 profile. The wing tips lie in the slipstream of the outer propellers and can be described similarly to the wing segments. The inverted V is assumed to lie in the freestream solely.

The lift, drag, and pitch moment coefficients for both used airfoil profiles over the angle of attack are shown in Fig. 2 using 180-degree polar approximations [35].

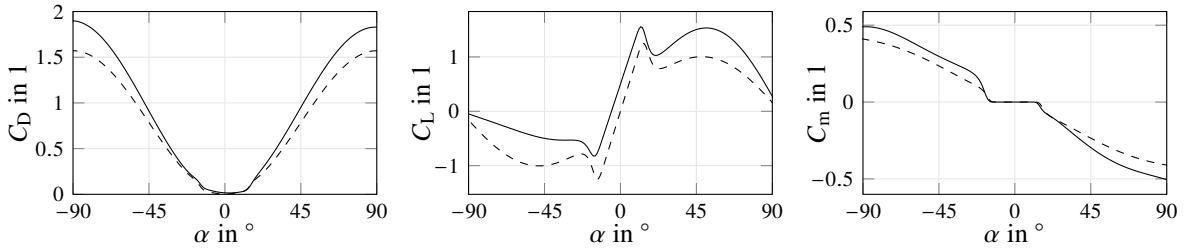


**Fig. 2** Lift  $C_L$ , drag  $C_D$ , and pitch moment  $C_m$  coefficients for the NASA GA(W)-2 (—) and the NACA-0009 (---) airfoil.

## E. Actuator Dynamics

The actuators represent the input dynamics for the tilt-angle, propellers, and control surfaces. The actuators are assumed to follow a second-order filter with saturations. The linear representation is

$$H(s) = \frac{\omega_0^2}{s^2 + 2\omega_0\zeta s + \omega_0^2} \quad (16)$$

The actuators are limited in terms of total deflection, rate, and acceleration. Upper limits are denoted as  $\bar{u}$  and lower limits as  $\underline{u}$ . The parameters assumed in the scope of this study are shown in Table 1.

**Table 1** Parameters of the actuator dynamics

		$\omega_0$	$\zeta$	$\bar{u}$	$\underline{u}$	$\bar{\dot{u}}$	$\underline{\dot{u}}$	$\bar{\ddot{u}}$	$\underline{\ddot{u}}$
Tilt angle	$\delta_w$	5 rad s <sup>-1</sup>	1	90°	0°	20° s <sup>-1</sup>	-20° s <sup>-1</sup>	20° s <sup>-2</sup>	20° s <sup>-3</sup>
Propeller speed	$n$	10 rad s <sup>-1</sup>	1	40 s <sup>-1</sup>	0 s <sup>-1</sup>	200 s <sup>-2</sup>	0 s <sup>-2</sup>	200 s <sup>-3</sup>	200 s <sup>-2</sup>
Control surface deflection	$\delta_e$	15 rad s <sup>-1</sup>	1	30°	-30°	30° s <sup>-1</sup>	-30° s <sup>-1</sup>	30° s <sup>-2</sup>	30° s <sup>-2</sup>

## F. Model Uncertainties

The uncertainties of the system are caused by the following effects [4, 34, 35, 37]:

- 1) Center of gravity and inertia changes with tilt angle and vehicle loading via additive uncertainties:  $|\Delta \mathbf{r}_{cg}^{\mathcal{B}}| \leq [0.2 \ 0.1 \ 0.1]^T$  m,  $|\Delta \mathbf{J}_{cg,xx}^{\mathcal{B}}| \leq 20$  kg m<sup>2</sup>,  $|\Delta \mathbf{J}_{cg,yy}^{\mathcal{B}}| \leq 20$  kg m<sup>2</sup>,  $|\Delta \mathbf{J}_{cg,zz}^{\mathcal{B}}| \leq 20$  kg m<sup>2</sup>,  $|\Delta \mathbf{J}_{cg,xz}^{\mathcal{B}}| \leq 5$  kg m<sup>2</sup>
- 2) Aerodynamics [3], especially effective slipstream velocity (thus, angle of attack) and post-stall behavior. These uncertainties can be considered by assuming an uncertain angle of attack in the argument of the coefficient functions, i.e.,  $C(\alpha^{\mathcal{W}} + \Delta\alpha^{\mathcal{W}})$ , where  $|\Delta\alpha^{\mathcal{W}}| \leq 1^\circ$  for  $|\alpha^{\mathcal{W}}| \leq 12^\circ$  and  $|\Delta\alpha^{\mathcal{W}}| \leq 2^\circ$  otherwise. Additionally, the aerodynamic coefficients of the fuselage have an additive uncertainty of  $|\Delta C^{\mathcal{B}}| \leq 0.2$ .
- 3) Actuator bandwidth during operations is uncertain, but using a conservative setting in Table 1 covers this.
- 4) Propeller aerodynamic coefficient over the envelope already covered in the input gain margin (and disk margin), as they primarily influence the effectiveness of the propellers.
- 5) Sensor delay is unknown, but covered in the analysis of the output phase margin (and disk margin).

## III. Flight Control System

The overall control architecture is shown in Fig. 3 and is characterized by a combination of dynamic inversion and control allocation, as well as the integration of attitude and flight path controllers. Furthermore, the switch between pilot inputs and autoflight functions allows for (partly) autonomous flights.

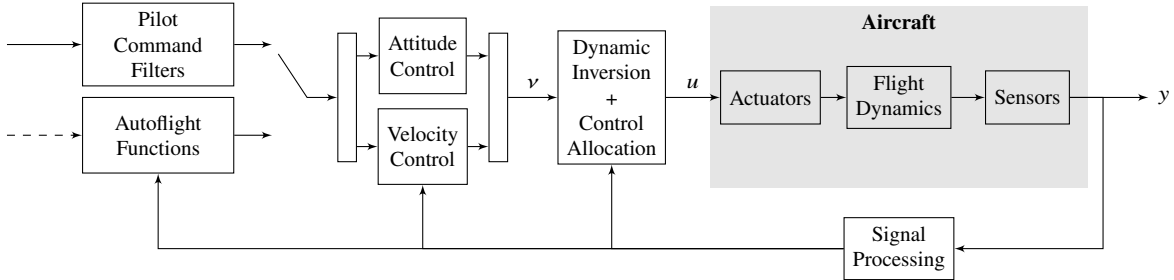


Fig. 3 Proposed control architecture for dynamic inversion-based tandem tilt-wing control.

The approach employs a hybrid NDI control law combined with an optimization-based control allocation, which inverts the rotational and translational dynamics in one to leverage specific vehicle characteristics [27].

The inversion is driven by the virtual control command  $\mathbf{v}^{\mathcal{B}} \equiv [\dot{\mathbf{v}}^{\mathcal{B}}, \dot{\boldsymbol{\omega}}^{\mathcal{B}}]$ . The high-level references provided by outer-loop guidance functions (or a pilot) are: The velocity in the control frame  $\mathbf{v}^{\mathcal{C}}$ , i.e., the NED frame rotated to the current heading, and the attitude  $\boldsymbol{\Theta}$ . To attain the virtual control commands, the following aspects have to be considered due to the unique configuration of the tandem tilt-wing aircraft:

- 1) Pitch attitude and tilt angle redundancy: Control over the longitudinal flight path can be exerted by both pitch attitude and tilt angle (cf. “pitch-supported tilting” [27]), motivating a pure pitch stabilization.
- 2) Interaction of lateral velocity and roll attitude, especially during hover: Rolling the vehicle rotates the thrust/lift vector, causing a sideward acceleration. This can be used to achieve lateral velocity control during hovering [25].
- 3) Flight mode-dependent lateral-directional allocation:
  - a) During thrust-borne flight, a heading angle ( $\psi$ ) and lateral velocity ( $v_y^{\mathcal{C}}$ ) are commanded.
  - b) During wing-borne flight, the control shifts towards a roll attitude command ( $\phi$ ) to execute coordinated turn maneuvers with sideslip (or lateral acceleration) stabilization ( $\beta = 0$ ).

## A. Hybrid Nonlinear Dynamic Inversion

For the state-space equation (1), and assuming full-state observation ( $h(x) = x$ ) and a linear low-pass filter function  $H_c(s)$ , the hybrid NDI law [27, 28] can be written implicitly as

$$g(\hat{x}, u) = \mathbf{v} - \mathcal{L}^{-1} \{H_c(s)\} * (\hat{x} - g(\hat{x}, \hat{u})) - \mathcal{L}^{-1} \{1 - H_c(s)\} * f(\hat{x}) =: \boldsymbol{\tau} \quad (17)$$

where  $\hat{\cdot}$  denotes estimated or measured quantities and by applying the inverse Laplace transformation  $\mathcal{L}^{-1}$ . The complementary filter is implemented in an integrated way with shared states between  $H_c(s)$  and  $(1 - H_c(s))$  as shown,

e.g., in [27–30]. Within the scope of this work, a first-order complementary filter is chosen, with a time constant  $\tau_{\text{compl}}$ .

For the tandem tilt-wing configuration, we invert the dynamics of  $\omega^{\mathcal{B}}$ ,  $\mathbf{v}_x^{\mathcal{B}}$ , and  $\mathbf{v}_z^{\mathcal{B}}$  from (1d) and (1c), which have a relative degree of 1. Note that we cannot control  $\mathbf{v}_y^{\mathcal{B}}$  directly in this aircraft configuration. Thus, for (17)

$$\mathcal{G}(\hat{x}, u) := \left[ \frac{1}{m} \mathbf{f}_x^{\mathcal{B}}(\hat{x}, u) \quad \frac{1}{m} \mathbf{f}_z^{\mathcal{B}}(\hat{x}, u) \quad \mathbf{J}_{\text{cg}}^{\mathcal{B}-1} \mathbf{m}^{\mathcal{B}}(\hat{x}, u) \right]^T \quad (18)$$

When using this design, zero dynamics exist, as only five degrees of freedom are controlled. While the x and z positions are controlled directly via the corresponding velocity, the velocity (and position) in the y direction is not addressed directly and can thus deviate uncontrolled. The dynamics of the y position  $\mathbf{r}_y^N$  position and velocity  $\dot{\mathbf{r}}_y^N$  can be approximated during hover as

$$\ddot{\mathbf{r}}_y^N = -C_{D_y} \dot{\mathbf{r}}_y^N - \frac{\mathbf{f}_{p,z}^N}{m} \sin \phi \quad (19a)$$

with a sideways drag coefficient  $C_{D_y}$ . This system is stable in the lateral translation. For the cruise flight, the lateral dynamics are dominated by the side slip angle  $\beta^{\mathcal{B}}$ , which is controlled through the yaw rate  $\omega_z^{\mathcal{B}}$ :

$$\dot{\mathbf{v}}_y^{\mathcal{B}} = \frac{1}{2} \rho \|\mathbf{v}^{\mathcal{B}}\|_2^2 C_{Y_\beta} \beta^{\mathcal{B}} \quad (19b)$$

$$\dot{\beta}^{\mathcal{B}} = \omega_z^{\mathcal{B}} \quad (19c)$$

Thus, the zero dynamics are stable or controllable, and therefore cannot deviate uncontrollably.

## B. Control Allocation

The general implicit equation (17) is solved for the input  $u$  by using local approximations employing the Taylor series expansion around an arbitrary expansion point  $u_0$  in combination with a control-allocation scheme. This approximation is similar to the incremental NDI law [39, 40] when used solely with a sensor-based NDI law, and it utilizes the currently measured control command as the expansion point, i.e.,  $u_0 = \hat{u}$ . A more detailed discussion on this topic is given in [30].

The optimization-based control allocation is discussed in detail in [26]. The objective is weighted least squares with the optimal control input  $\mathbf{u}^*$  being a design decision, commonly chosen close to the current control deflection, and in this work, as

$$u_0 = [\bar{\delta}_{w1..2}, 0.95\bar{n}_{1..4}, 0.95\bar{n}_{5..8}, 0]$$

with the mean operator  $\bar{\cdot}$ . The final control allocation law in this case, with the weighting matrix  $\mathbf{W}$ , is [26]

$$\mathbf{u} = \mathbf{B}^+ \boldsymbol{\tau} + (\mathbf{I} - \mathbf{B}^+ \nabla_u \mathcal{G}(\hat{x}, \mathbf{u}_0)) \mathbf{u}^* = \mathbf{u}^* + \mathbf{B}^+ (\boldsymbol{\tau} - \nabla_u \mathcal{G}(\hat{x}, \mathbf{u}_0) \mathbf{u}^*) \quad (20)$$

with the weighted pseudo-inverse  $\mathbf{B}^+ = \mathbf{W} \nabla_u \mathcal{G}(\hat{x}, \mathbf{u}_0)^T \left( \nabla_u \mathcal{G}(\hat{x}, \mathbf{u}_0) \mathbf{W}^{-1} \nabla_u \mathcal{G}(\hat{x}, \mathbf{u}_0)^T \right)^{-1}$  and the right-hand side of (17)  $\boldsymbol{\tau}$ . A detailed discussion of the design of an optimization-based control allocation in combination with dynamic inversion for transformational eVTOLs is provided in [8, 26], and for other configurations in [41, 42].

The inverse function theorem states that (18) can be solved for  $u$  in a neighborhood of a given  $u_0$  and  $x_0 = \hat{x}$ , if  $\nabla_u \mathcal{G}(\hat{x}, \mathbf{u}_0)$  is invertible. Thus, the control effectiveness matrix  $\nabla_u \mathcal{G}(\hat{x}, \mathbf{u}_0)$  must be non-singular throughout the entire flight envelope. This is subsequently argued, first physically and then numerically, using a specific trajectory.

The control-effectiveness matrix  $\nabla_u \mathcal{G}(\hat{x}, \mathbf{u}_0)$  retains full rank in every flight regime because the actuators contribute independently to all five degrees of freedom, as shown in Table 2. This, however, assumes that the gradient of the forces and moments with respect to the appropriate control input does not vanish. However, especially for the thrust and tilt angle, this means that they do not saturate, which can be ensured by appropriately restricting the achievable flight envelope.

Numerically, this can be analyzed and verified through the least singular value and the numerical condition number. The minimum singular value  $\sigma_{\min}$  and the condition number  $\kappa = \frac{\sigma_{\max}}{\sigma_{\min}}$  are shown for the leveled transition maneuver in Fig. 4.

## IV. Robust Analysis and Synthesis

The main contribution of this work is the robust analysis of the proposed control law. As these inherently nonlinear configurations are complex in nature, the analysis process must be carefully thought out. The requirements for the

**Table 2 Primary control mechanisms for the five axes in the three flight regimes.**

Axis	Hover (thrust-borne)	Transition	Cruise (wing-borne)
$f_x^B$	tilt angle tilting the thrust vector	Combination of the independent control inputs thrust and tilt angle	total thrust tilt angle tilting thrust vector and increasing angle of attack
$f_z^B$			
$m_y^B$	differential thrust front-rear	differential thrust front-rear and elevon deflection	diff. thrust front-rear (vertical separation of wings) or elevon deflection
$m_x^B$	differential thrust left-right	Combination of the independent control inputs elevon deflection and diff. thrusts	elevon deflection or diff. thrust pos./neg. rotating
$m_z^B$	diff. thrust pos./neg. rotating or elevon slipstream deflection		

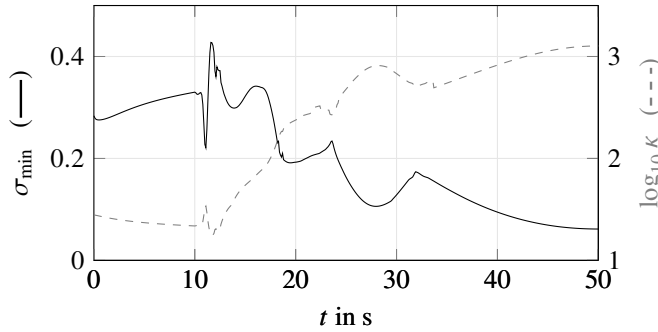


**Fig. 4 Minimum singular value and condition number of the control effectiveness matrix along transition [27]**

system are that stability must be guaranteed throughout all flight phases for the closed-loop system, including a certain level of robustness to uncertainties. The means of compliance are selected to be the  $\mu$ -analysis and (worst-case) disk margins along the trim trajectory and accelerated and decelerated trim trajectories. This approach, however, does not include more complex dynamic operating points [35] but already covers an extensive range of the flight envelope and guarantees trimmed flight points throughout, thereby avoiding departure. Furthermore, after defining means of compliance regarding robustness and stability, it is crucial to incorporate them into the synthesis process. Otherwise, the rating would not be fair. Thus, after defining the robustness metrics, a fixed-structure parameter synthesis is performed, optimizing robustness and performance criteria in the multi-objective parameter synthesis framework MOPS [43].

### A. Integrated Linear Representation

To analyze the system using  $\mu$ -analysis, the system is represented in the  $\Delta - P - K$  form by separating the system into the plant  $P(s)$ , representing of the 6-DoF flight dynamics with the aerodynamic and propulsive forces and moments with the uncertainties of the plant  $\Delta_p(s)$ ,  $\|\Delta_p\|_\infty \leq 1$ , the controller  $K(s)$ , that tracks a reference providing the plant outputs under the presence of actuator dynamics  $G(s)$ .

The representation shown in Fig. 5 of the system is used, where  $y = [y_r, x, u]$  denotes the measurements of the tracking variable  $y_r$  and the remaining states  $x, u$  the control inputs,  $w$  the disturbances, and  $z$  the performance signals.

The closed-loop system  $M$  and the systems  $P, K,$  and  $G$  are

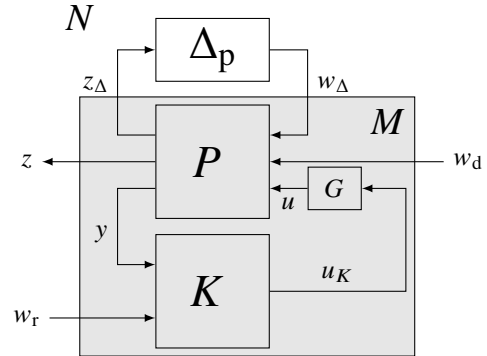


**Fig. 5 Diagram of the linear closed-loop system**

represented by:

$$\begin{bmatrix} z_\Delta \\ z_y \\ y \end{bmatrix} = \underbrace{\begin{bmatrix} P_{11} & P_{12} & P_{13} \\ P_{21} & P_{22} & P_{23} \\ P_{31} & P_{32} & P_{33} \end{bmatrix}}_P \begin{bmatrix} w_\Delta \\ w_d \\ u \end{bmatrix}, \quad u_K = \underbrace{\begin{bmatrix} K_{11} & K_{12} \end{bmatrix}}_K \begin{bmatrix} y \\ w_r \end{bmatrix}, \quad u = G u_K, \quad \begin{bmatrix} z_\Delta \\ z_y \end{bmatrix} = \underbrace{\begin{bmatrix} M_{11} & M_{12} & M_{13} \\ M_{21} & M_{22} & M_{23} \end{bmatrix}}_M \begin{bmatrix} w_\Delta \\ w_d \\ w_r \end{bmatrix}$$

The closed-loop system  $M$  can be determined by using the lower linear fractional transformation (LFT) as  $M = \mathcal{F}_l(P, G K)$ . Using the upper LFT  $\mathcal{F}_u$ , the full system  $N = \mathcal{F}_u(M, \Delta)$  can be described.

## B. Robustness: $\mu$ -Analysis and Worst-Case Disk Margins

Based on the above system, the metrics for robustness used in this work can be determined. Robustness will be quantified using the stability margin based on the structured singular value  $\mu$  and the worst-case multiloop and loop-at-a-time disk margins  $\alpha_{\max}$  and  $\alpha_{\max,i}$  at the input  $i$  and the output  $o$ , as well as the corresponding gain and phase margins ( $\gamma_{\min}, \gamma_{\max}$ ) and  $\phi_m$ . Consider a structured multiplicative uncertainty  $\Delta$  belonging to the normalized disk set

$$\Delta = \{\Delta \in \mathbb{C} : |\Delta| < 1\}.$$

with the structure  $\Delta = \text{diag}(\delta_1, \dots, \delta_N)$ . The uncertainties are taken from Section II.F.

**Structured Singular Value  $\mu$  [44]** The Structured Singular Value  $\mu$  can be used to quantify the robustness of the system and is defined as

$$\mu_\Delta(M)^{-1} = \min_{\Delta \in \Delta} \{\bar{\sigma}(\Delta) : \det(I - M \Delta) = 0\} \quad (21)$$

where  $\bar{\sigma}$  denotes the largest singular value. This can be thought of as the reciprocal of how big that structured uncertainty  $\Delta$  can be before the matrix  $I - M\Delta$  becomes singular. Nominal stability and performance are guaranteed if  $M$  is internally stable and  $|M_{22}|_\infty < 1$ . Then, robust stability and performance are guaranteed if  $\mu_\Delta(N_{11}) < 1, \forall \omega$  and  $\mu_{\tilde{\Delta}}(N) < 1, \forall \omega, \tilde{\Delta} = \text{diag}(\Delta, \Delta_P)$ . A more detailed explanation is provided, for example, in [44].

**Worst-Case Disk Margin [31]** Consider the nominal open-loop transfer function for the input margins  $L_i$  and output margins  $L_o$ , where  $L_i \equiv K P G$  and  $L_o \equiv P G K$ , and the set of perturbations

$$D_\sigma(\alpha) = \left\{ \frac{1 + \frac{1-\sigma}{2}\delta}{1 - \frac{1+\sigma}{2}\delta} : \delta \in \mathbb{C} \text{ with } |\delta| < \alpha \right\}$$

where  $\sigma$  is the skew parameter (nominally  $\sigma = 0$ ). The perturbed loop transfer functions are  $L \cdot \text{diag}(F_1, \dots, F_N)$  for  $F_i \in D_\sigma(\alpha)$  where  $\alpha > 0$  scales the uncertainty magnitude. The worst-case disk margin  $\alpha_{\max}$  is defined as the largest value of  $\alpha$  such that the closed loop with the perturbed loop transfer function is stable for all  $F_i \in D_\sigma(\alpha)$ . This is equal to

$$\alpha_{\max} = \inf \left\{ \alpha > 0 : \forall F_i \in D_\sigma(\alpha), \det(I + L \cdot \text{diag}(F_1, \dots, F_N)) = 0 \right\} \quad (22)$$

This problem can be solved using the structured singular value ( $\mu$ ) [31]. For MIMO systems, the worst-case disk margin can be quantified for the multiloop or loop-at-a-time case, where either all feedback channels are perturbed simultaneously, or just one channel (i.e., a single  $F_i$ ) is perturbed while fixing all other channels. The multiloop simultaneous variations across all loops provide a more conservative robustness assessment than sequential loop-at-a-time analysis [31].

The worst-case minimum and maximum gain- and phase margins can be determined as [31]

$$\gamma_{\min} = \frac{2 - \alpha_{\max} (1 - \sigma)}{2 + \alpha_{\max} (1 + \sigma)}, \quad \gamma_{\max} = \frac{2 + \alpha_{\max} (1 - \sigma)}{2 - \alpha_{\max} (1 + \sigma)}, \quad \cos \phi_m = \frac{1 + \gamma_{\min} \gamma_{\max}}{\gamma_{\min} + \gamma_{\max}}$$

### C. Robust Synthesis of Controller Gains

To provide a fair assessment of the system's robustness and stability, the controller must be synthesized with these criteria in mind. Thus, a multi-objective parameter synthesis of the fixed-structure controller gains with respect to robustness and performance is done.

The objectives are:

- 1) on the nonlinear simulation flying transition trajectories [4]
  - a) minimize control activity
  - b) maximize disturbance rejection
  - c) minimize tracking error (i.e., settling time and overshoot)
- 2) on linearized systems at multiple operating points along the accelerated, static, and decelerated trim lines
  - a) maximizing the worst-case disk margins
  - b) maximizing the stability margins
  - c) minimizing the tracking error (i.e., settling time and overshoot)
  - d) minimizing the disturbance transfer  $\|G_{d \rightarrow z}\|_{\infty}$

The setup is built using the software MOPS [43].

## V. Results: Open-Loop Analysis

The vehicle is analyzed without a controller first to attain an understanding of its dynamic behavior. Therefore, a trim study to determine the (trimmed) operating points is carried out. Afterward, the stability of the open-loop system is analyzed at the determined operating points. The analysis reveals that the vehicle exhibits unstable poles throughout its flight envelope, particularly during the transition.

### A. Operating Points and Characteristics of the Statically Trimmed Tilt-Wing

The characteristics of the tilt-wing VTOL can be analyzed by employing a trim study. The maximum speed of the aircraft is reached at approximately  $70 \text{ m s}^{-1}$ . As presented in [2, 34, 35], the tilt-wing exhibits a characteristic trim curve. This "S"-shape originates from the stall characteristics of the airfoil as the aircraft traverses the stall during the static trim transition.

The aircraft is trimmed for a level, straight forward flight with minimal total power consumption according to the control allocation objective. The results of the optimization are presented in Fig. 6 as the trim curve.

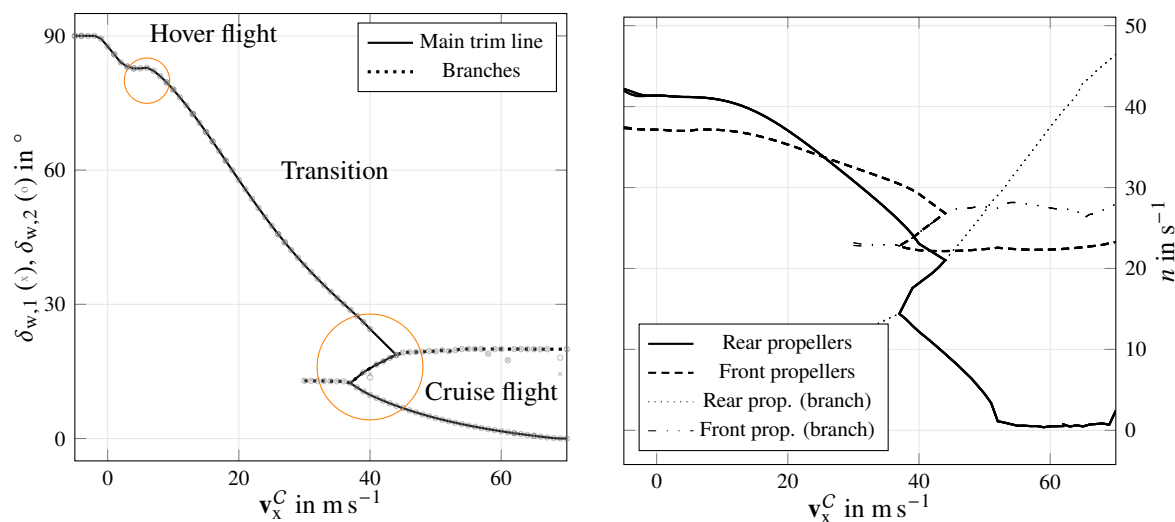


Fig. 6 Static trim curve for leveled flight.

Evidently, the flight phases of a tilt-wing aircraft can be distinguished into three distinct phases, during which different physical phenomena prevail.

**Hover flight** During hover flight, the aircraft is propulsion-dominated or thrust-borne and behaves similarly to a multicopter. Steady hover flight is at  $v_x^C = 0 \text{ m s}^{-1}$ , but the hover regime spans  $-5 \text{ m s}^{-1} \leq v_x^C \leq 10 \text{ m s}^{-1}$  as shown in Fig. 6.

**Cruise flight** During cruise flight, the aircraft is primarily influenced by aerodynamic forces and moments, behaving similarly to a fixed-wing aircraft, i.e., wing-borne. The thrust is used to compensate for drag and to produce moments through differential thrust. The nominal cruise flight is at  $v_x^C = 65 \text{ m s}^{-1}$ , where the tilt angles are essentially at  $0^\circ$ . The cruise region is in  $37 \text{ m s}^{-1} \leq v_x^C$  and  $\delta_w \leq 12^\circ$ .

**Transition flight** During the acceleration/deceleration phase, the aircraft stops behaving distinctly as in the other phases and enters a blended phase. During this phase, the aircraft can and may enter post-stall regimes, governed by more complex interactions and changing dynamics.

Additionally, trim line *branches* exist in Fig. 6. They are a local minimum of the optimization objective and correspond to the valley in the post-stall lift curve. Although they are valid trim points, they are not relevant for the flight operation, as they result in less optimal flight conditions, which can even be disadvantageous.

However, dynamic transition analysis shows that this can be avoided by specific transition maneuvers, as, e.g., shown in [4].

## B. Accelerated and Decelerated Trimmed Tilt-Wing

To cover a larger part of the envelope and to smooth the unsteady parts in the transition trim trajectory, dynamic transition maneuvers must be considered [4]. Thus, the vehicle is trimmed along its flight speeds for an accelerated and decelerated case. The magnitudes  $\pm 0.1 g$  are chosen to cover a large part of the trajectory and are in alignment with [4].

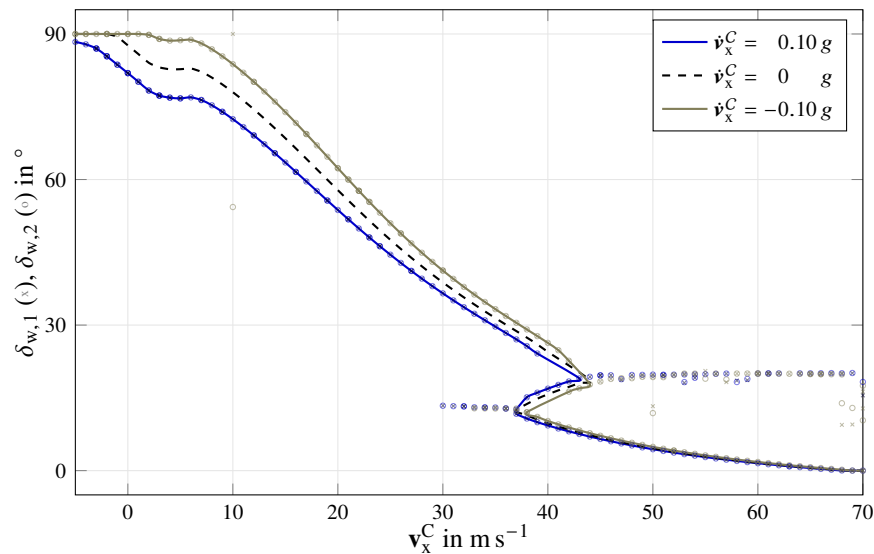


**Fig. 7 Accelerated and decelerated trim curve for level flight.**

The results are shown in Fig. 7 and follow a similar trend to the static reference. While the hover trim lines deviate, the cruise trim lines align for the considered cases. Furthermore, the operation points also allow the argumentation from [4] that dynamic maneuvers in the form of acceleration or deceleration help to overcome the “S” shape of the trim curves.

For the analysis, the points lying on the smooth lines in Fig. 7 are investigated.

## C. Stability Analysis

The system can be linearized along the transition trajectory shown in Fig. 6. The result is depicted in Fig. 8, which shows that the system has unstable poles throughout the envelope. Similar results have been found in [45].

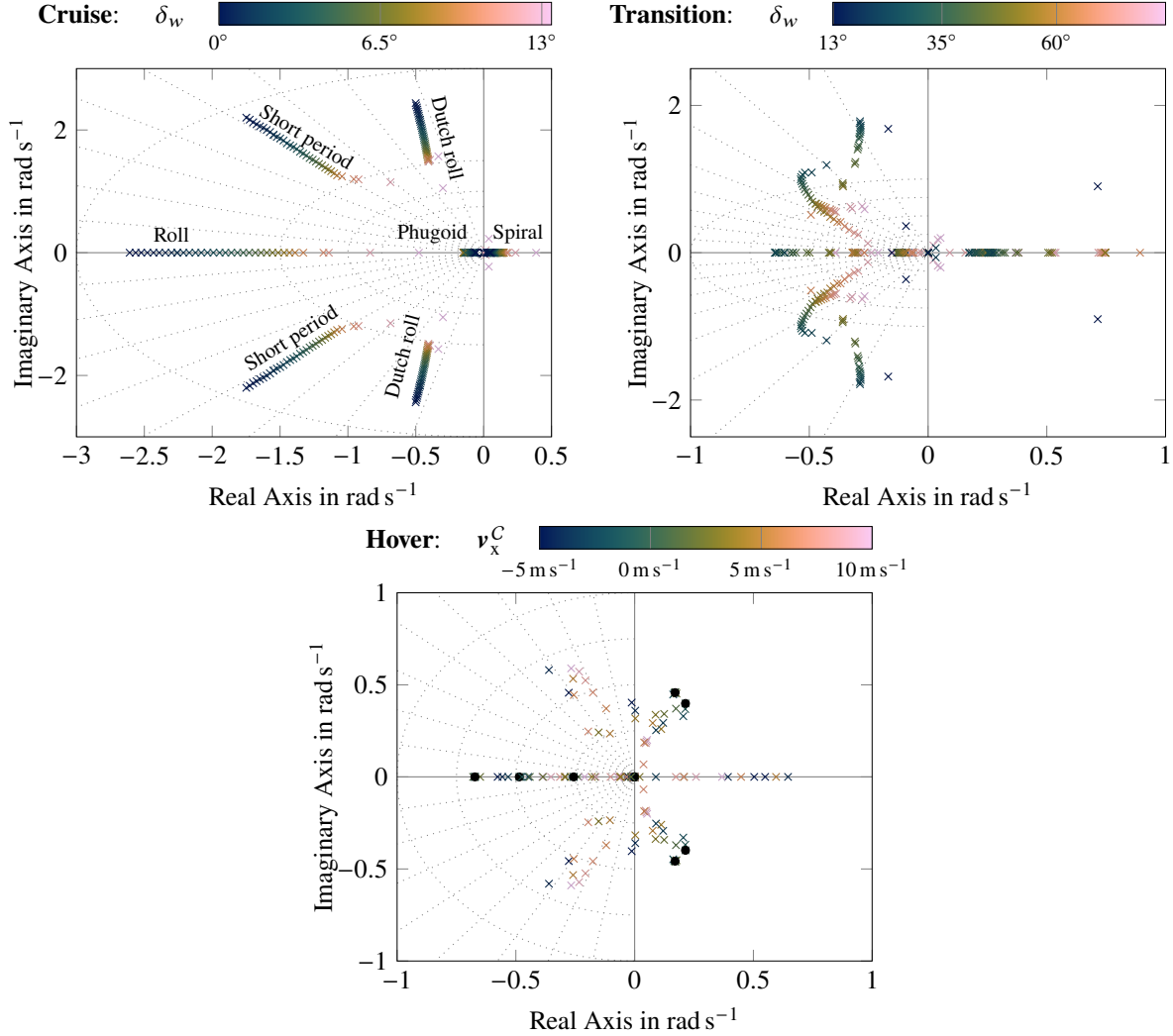


**Fig. 8** Open loop poles of the linearized system along the trim trajectory (cf. Fig. 6) for the three different flight modes.

**Cruise flight** During cruise flight, the aircraft behaves similarly to a fixed-wing aircraft. This is visible in Fig. 8. The dynamics can be similarly characterized into the longitudinal phugoid and short-period modes, as well as the lateral roll, spiral, and Dutch roll modes. The spiral mode is unstable in this configuration, and the phugoid model becomes marginally stable or unstable in certain flight phases, particularly near the transition.

**Hover flight** During hover flight, the aircraft is inherently unstable. An unstable coupling of rotations and translations characterizes the dynamics. As indicated in Fig. 8, increasing the velocity, thereby increasing the aerodynamic interaction, gradually stabilizes the system. The dampening effect of the airflow causes this. The poles of the  $v_x^C = 0 \text{ m s}^{-1}$  case are highlighted in Fig. 8 by a black dot.

**Transition flight** The aircraft's behavior transitions from hover to cruise characteristics. This can also be identified in the movement of the poles in Fig. 8.

## VI. Results: Closed-Loop Analysis

The closed-loop stability and robustness are analyzed by first examining the main static flight regimes, i.e., hover and cruise flight conditions, and then investigating the static transition maneuvers between them. Afterward, the accelerated and decelerated transition maneuver is investigated. Table 3 shows the lowest margins in each static flight phase and thus represents a more conservative estimate. These results indicate that the controller can stabilize the system throughout all flight phases and under the assumed uncertainties. Furthermore, sufficient disk margins are provided at the output. However, the disk margins at the input are relatively narrow. The argumentation applies to all cases since the methods used give conservative estimates, especially the worst-case multiloop disk margin. Multiple solutions contained a large spread between the upper and lower bounds, indicating a low estimate. Furthermore, especially during cruise flight, the lowest margin is achieved at flight speeds above the nominal cruise flight speed. However, there are also systematic reasons for low disk margins, i.e., the susceptibility of NDI methods to actuator uncertainties and phase lags. Although hybrid NDI improves robustness in this regard, it still relies on synchronized actuator measurements.

The results are shown and explained in detail below. The overall results indicate that the larger uncertainties in aerodynamics result in narrow margins during the transition and cruise phases, whereas the hover case exhibits wider margins. Furthermore, for the dynamic transition maneuvers, an unstable region in the backward or decelerating transition is identified. By adapting the deceleration, this instability can be avoided. Thus, the backward transition has to be performed carefully in the low-speed region.

In the following, the disk margins are annotated with the corresponding maximum gain and phase margin for a clearer presentation. Furthermore, data points where the robust analysis solver did not converge have been filtered out to reduce outliers. Additionally, for data points where the lower and upper bound estimation deviates a lot, both values are shown to indicate that the estimation might be overly conservative.

**Table 3 Minimum of nominal/worst-case multiloop disk margins and stability margins of the static flight phases.**

	Hover	Cruise	Transition
Nominal disk margin on output	0.7 (6.35 dB, 38.58°)	0.7 (6.35 dB, 38.58°)	0.7 (6.35 dB, 38.58°)
Nominal disk margin on input	0.62 (5.57 dB, 34.45°)	0.62 (5.57 dB, 34.45°)	0.25 (2.18 dB, 14.25°)
Worst-case disk margin on output	0.69 (6.25 dB, 38.07°)	0.6 (5.38 dB, 33.4°)	0.6 (5.38 dB, 33.4°)
Worst-case disk margin on input	0.6 (5.38 dB, 33.4°)	0.2 (1.74 dB, 11.42°)	0.21 (1.83 dB, 11.99°)
Stability margin (lower bound)	4.3	1.47	1.8

### A. Hover Flight Regime

The vehicle is inherently unstable in hover flight. The prevailing uncertainties are in the weight and balance system and the inputs and outputs. The results show that the controller can effectively stabilize the vehicle and exhibits sufficient robustness against the uncertainties. The poles of the closed-loop system in hover conditions are shown in Fig. 9, demonstrating stable behavior even in the presence of uncertainties.

The robustness boundaries of the system are depicted in Fig. 10. At  $v_x^C = 0 \text{ m s}^{-1}$ , the input worst-case disk margin is at 0.61 (5.47 dB, 33.92°) and the output worst-case disk margin is at 0.7 (6.35 dB, 38.58°). Both are roughly equal to the nominal disk margins. The robust stability margin has a guaranteed lower bound of 10.5 in this case, indicating that the controller can effectively cope with uncertainties beyond the assumed ones. This proves stable behavior with sufficient margins against the selected uncertainties in the closed-loop hover condition.

For the whole hover regime, Fig. 10b shows constant margins throughout. The stability margin remains above 4.3. But this included the backward flight. When considering only forward flight, the stability margins stays above 8.0. The worst-case disk margins at the output remain at around 0.7 (6.35 dB, 38.58°), while those at the input approach 0.6 (5.38 dB, 33.4°). The nominal disk margins have a similar magnitude and also stay constant throughout this flight phase. All these aspects suggest that, strengthened by being a conservative lower estimate, the system has sufficient robustness in the hover flight phase.

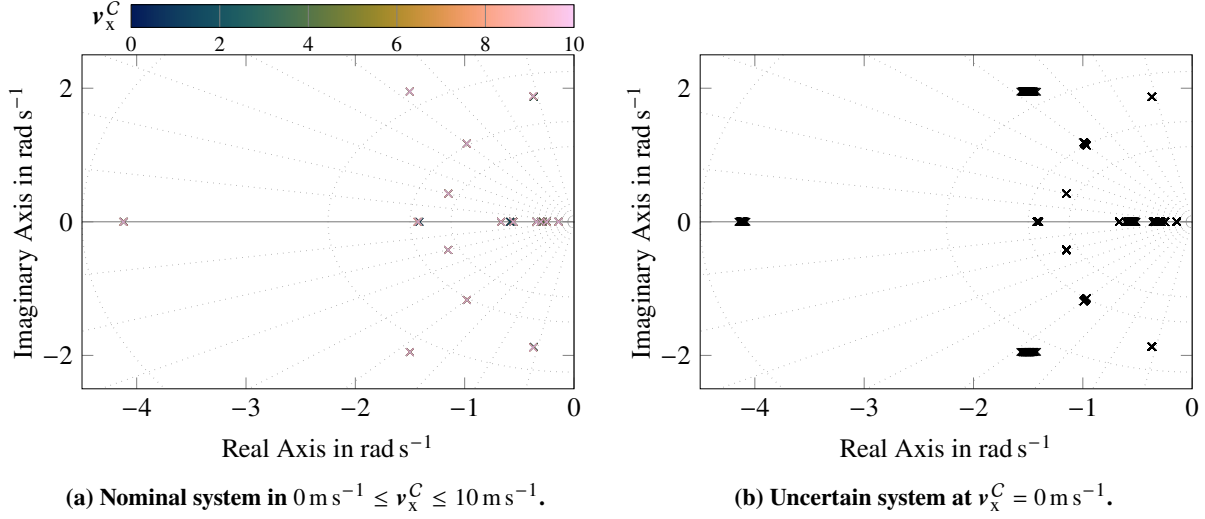


**Fig. 9 Pole-zero map of closed-loop hover flight.**

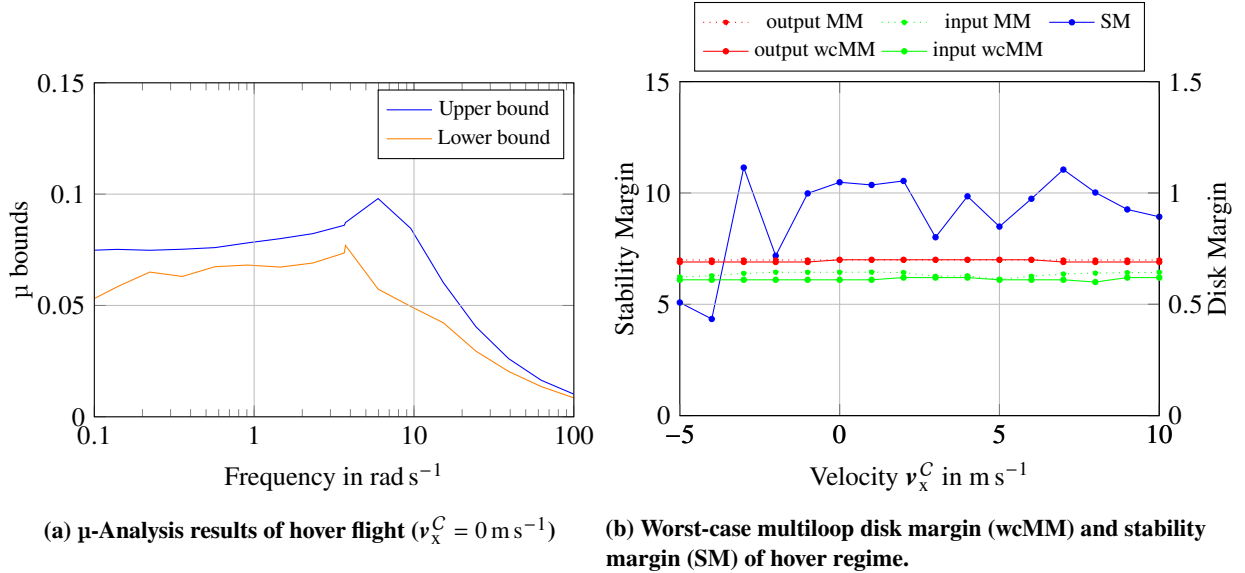


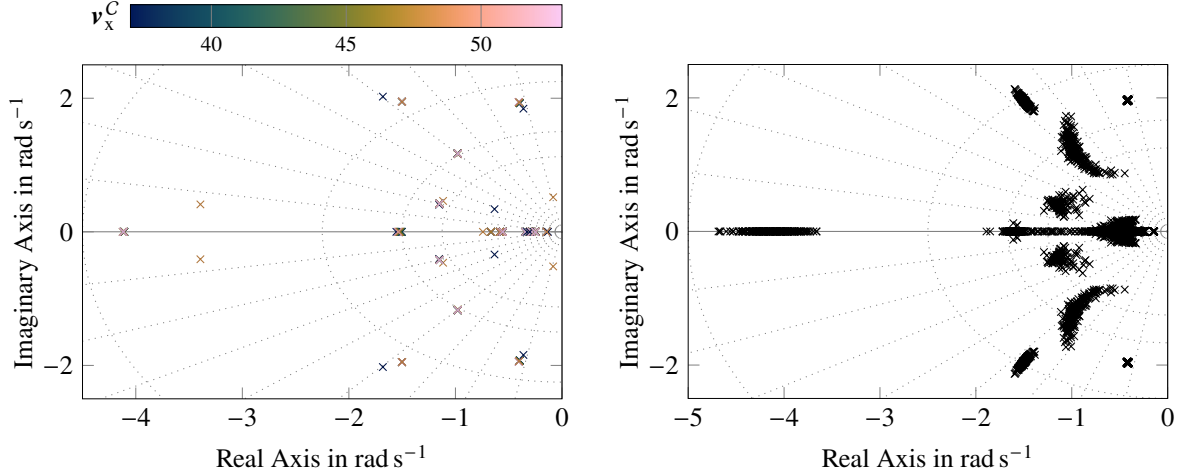
**Fig. 10 Margins of the uncertain closed-loop system in hover flight ( $0 \text{ m s}^{-1} \leq v_x^C \leq 10 \text{ m s}^{-1}$ ).**

## B. Cruise Flight Regime

During cruise flight, the open-loop systems stabilize more, leaving only an unstable spiral pole (cf. Section V). As shown in Fig. 11, the controller stabilizes the system throughout the cruise regime (a) and in the presence of the assumed uncertainties (b). However, the uncertainties influence the locations of the poles more strongly in this case than in the hover case due to the increased aerodynamic influence. As the velocity increases, the stability margins decrease, with the input margins being the primary factor.

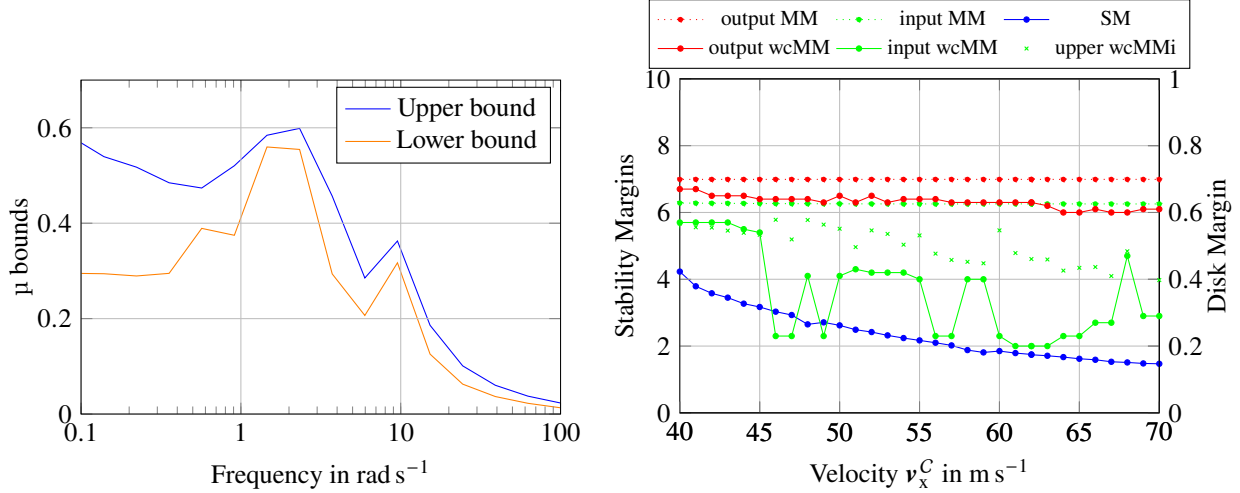
At  $65 \text{ m s}^{-1}$ , the robust stability margin has a lower bound of 1.62. The worst-case disk margins are 0.25 (2.18 dB,  $14.25^\circ$ ) at the input and 0.62 (5.57 dB,  $34.45^\circ$ ) at the output for the nominal cruise speed. The nominal output disk margin is at 0.7 (6.35 dB,  $38.58^\circ$ ), while the nominal input disk margin is at 0.62 (5.57 dB,  $34.45^\circ$ ). This shows that the input disk margin is more susceptible to uncertainties and the worst case.

Throughout the cruise regime, the stability margin has a minimal value of the lower bound of 1.47. This proves that the closed-loop system can effectively cope with the assumed uncertainties and still maintain some margin. As most uncertainties concern aerodynamics, which prevail during cruise flight and make only a minor contribution during hover



(a) In cruise regime  $37 \text{ m s}^{-1} \leq v_x^C \leq 70 \text{ m s}^{-1}$  and  $0^\circ \leq \delta_w \leq 13^\circ$  without uncertainties. (b) At cruise point  $v_x^C = 65 \text{ m s}^{-1}$  with uncertainties.

**Fig. 11 Pole-zero map of closed-loop cruise flight.**



(a)  $\mu$ -Analysis results at  $v_x^C = 65 \text{ m s}^{-1}$

(b) Worst-case multiloop disk margin (wcMM) and stability margin (SM) of cruise regime.

**Fig. 12 Margins of the uncertain closed-loop system in cruise flight ( $40 \text{ m s}^{-1} \leq v_x^C \leq 70 \text{ m s}^{-1}$ ).**

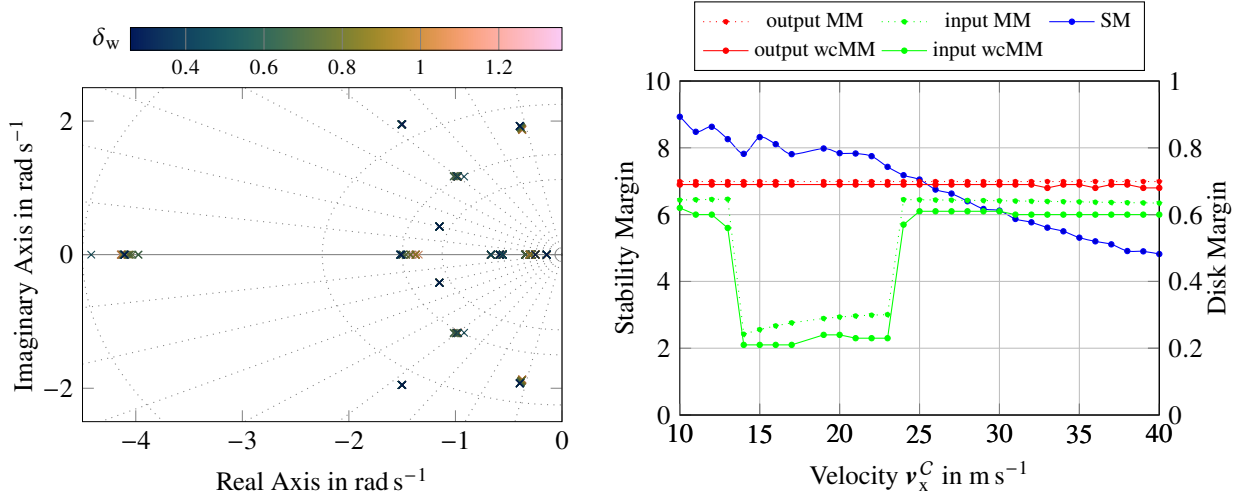
flight, it is expected that the stability margin is significantly lower during cruise flight compared to hover flight and, additionally, that the stability margin decreases with increasing velocity.

A closer look at the disk margins shown in Fig. 12 b shows a nominal disk margins throughout the cruise regime of 0.62 (5.57 dB, 34.45°) at the input and 0.7 (6.35 dB, 38.58°) at the output. Both values guarantee sufficient margins, as they represent a conservative estimation. The worst-case disk margin on the output remains relatively constant with a minimum at 0.6 (5.38 dB, 33.4°). The worst-case input disk margin fluctuates, but stays above 0.2 (1.74 dB, 11.42°). Thus, even with the conservative estimations carried out in this study, the system provides robustness in the worst-case. Additionally, the fluctuations are caused by a large spread between the lower and upper bound of the estimate (denoted with a green cross). Although, this the real value can be anywhere within these boundaries, larger spreads often have a more conservative lower bound.

All these aspects suggest that, strengthened by being a conservative lower estimate, the system should have sufficient robustness in the cruise flight phase.

### C. Static Transition Flight

After thoroughly examining the main flight phases, cruise and hover, the transition between these phases is analyzed as the critical flight phase. The static transition trajectory is derived in Section V.A and depicted in Fig. 6. During transition, the worst-case disk margins follow the trend of the nominal ones. This indicates, that the uncertainties of the plant do not influence the system too much. Actually, the combination of thrust- and wing-borne flight makes the vehicle less susceptible to uncertainties in the aerodynamics. However, the stability margin decreases as the aircraft transitions from thrust-borne to wing-borne flight as shown in Fig. 13b, but always stays above 4.4. During low-speed transition, the input disk margins decrease drastically because the wing reaches or passes the stall line of the airfoil in this region.



(a) Pole-zero map of the closed-loop system in the static transition regime. (b) Worst-case multiloop disk margin (wcMM) and stability margin (SM) of transition phase.

**Fig. 13** Closed-loop system along the static transition trajectory

The disk margin at the input is roughly at 0.64 (5.76 dB, 35.49°) in the nominal case, except during the low-speed transition, where the values falls to 0.25 (2.18 dB, 14.25°). The worst-case disk margin follows this trend and reaches a minimum of 0.21 (1.83 dB, 11.99°) during the low-speed transition but stays at 0.6 (5.38 dB, 33.4°) elsewhere. Meanwhile, the output disk margin is roughly constant throughout at 0.7 (6.35 dB, 38.58°) for the nominal case and 0.68 (6.15 dB, 37.56°) for the worst-case. Fig. 13 shows the static transition corridor without the “backside of the S-curve” (cf. Section V). In this region, all margins are reduced and reach a minimum for the worst-case disk margin of 0.6 (5.38 dB, 33.4°) for the output and 0.3 (2.63 dB, 17.06°) for the input. The minimal stability margin reaches 1.8.

The results indicate that the vehicle is only slightly susceptible to uncertainties during the transition. A reason for this could be the combination of propulsive and aerodynamic inputs, which enable distinct and improved handling of the vehicle. The trend of the stability margin is gradually decreasing, reflecting the influence of aerodynamic uncertainties as the aircraft approaches the aerodynamic flight regime. The transition does not compromise the robustness of the controller more than the cruise flight. All these aspects suggest that, strengthened by being a conservative lower estimate, the system has sufficient robustness during transition. Additionally, the flight control design originates from a fixed-wing flight control structure and, through these results, proves to handle both hover and transition phases well, too. Nevertheless, the low-speed phase needs to be considered carefully.

### D. Accelerated/Decelerated Flight

To linearize the accelerated and decelerated flight, it is important to find an operating point for the controller where  $\mathbf{u} = \hat{\mathbf{u}}$ , i.e., the command output from the controller should align with the current control allocation. Otherwise, a reallocation would take place, which disturbed the linear assumption and leads to unsuitable results.

The results in Fig. 14b indicate that the forward or accelerated transition has similar robustness and stability properties as the static case. Indeed, good-natured slipstream effect [4] even prevents the small input disk-margins in the low-speed transition regime. However, the large spread between the lower and upper bound (depicted by the green crosses) of the worst-case input disk margins leads to a low minimum of 0.19 (1.65 dB, 10.85°). In contrast, the nominal

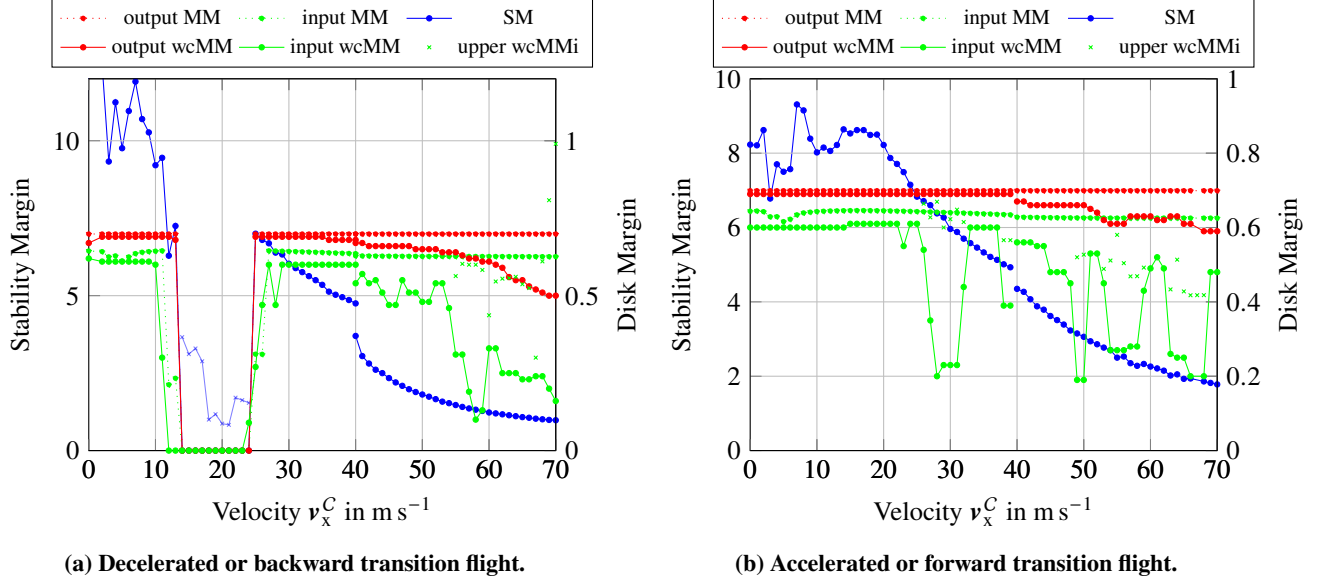


**Fig. 14** Worst-case multiloop disk margin (wcMM) and stability margin (SM) of accelerated and decelerated transition phase.

input disk margin stays above 0.6 (5.38 dB,  $33.4^\circ$ ), the worst-case output disk margin above 0.59 (5.28 dB,  $32.87^\circ$ ), and the nominal output disk margin above 0.7 (6.35 dB,  $38.58^\circ$ ). The stability margin decreases, similar to the static case, with increasing velocity to 1.8. The minimal worst-case margins during the “S” flight phase are 0.59 (5.28 dB,  $32.87^\circ$ ) on the output, 0.19 (1.65 dB,  $10.85^\circ$ ) on the input, and 2.0 for the stability margin. Thus, the closed-loop system remains stable with sufficient robustness during the forward transition. Furthermore, it confirms the good-nature of this maneuver [4] as the robustness compared to the static transition maneuver increases. However, large spreads between lower and upper bound are present and lead to a less precise result.

The backward or decelerated transition in Fig. 14a shows a less robust behavior and is even unstable during the low-speed transition (around  $13 m s^{-1}$  to  $23 m s^{-1}$ ). This is caused by high angles of attack required during this maneuver in combination with the absence of beneficial aero-propulsive effects. Thus, the system cannot decelerate with the assumed acceleration in this range in a stable way. However, when looking at the closed-loop system for a smaller deceleration ( $\dot{v}_x^C = -0.05g$ ), the closed-loop system becomes stable again. This additional case is depicted in Fig. 14a by the blue crosses. The aircraft then has a stability margin of above 0.9. Hence, the system is stable with some margin when considering a slower deceleration maneuver within the low-speed transition regime. This motivates a more careful handling and investigation of the backward transition, including the incorporation of optimized transition maneuvers for the backward transition into the control design [4]. The backward transition in the other flight regimes has a stability margin above 1.0 with the lowest value at  $70 m s^{-1}$ . The output disk margin stays above 0.7 (6.35 dB,  $38.58^\circ$ ) for the nominal case and above 0.5 (4.44 dB,  $28.07^\circ$ ) for the worst-case. The input disk margin has a lower bound of 0.62 (5.57 dB,  $34.45^\circ$ ) for the nominal case and 0.1 (0.87 dB,  $5.72^\circ$ ) for the worst case. However, the upper bound for the worst-case input disk margins again deviates strongly from the lower bound.

Recapitulatory, the forward transition has a positive influence on the stability and robustness of the system, while the backward transition can cause instabilities and has to be considered carefully.

## VII. Conclusion

In this study, we have presented a closed-loop stability and robustness analysis of a dynamic inversion-based control architecture for a tilt-wing electric VTOL aircraft. We have proposed initial means of compliance to validate the stability and robustness of the resulting system based on linear stability and robustness metrics. The structured singular value  $\mu$  and the (worst-case) disk margin are used to quantify the robustness properties of the closed-loop system. The proposed framework has been defined and applied to the tandem tilt-wing eVTOL configuration. The system has been analyzed at trimmed points throughout the envelope. The controller proved capable of decoupling and stabilizing the complex and

unstable dynamics under both nominal and perturbed conditions. The proposed control law maintains stable flight across the full envelope of wing-tilt angles and tolerates sufficient model uncertainties. However, the decelerated or backward transition needs to be handled carefully in the low-speed regime to provide stable behavior.

However, the proposed approach also has shortcomings in the clearance of flight control laws for tilt-wing aircraft. Those are inherent to the structured singular value and disk margin, as for both, the worst-case always lies in a corner of the uncertainty space. Furthermore, the multiloop margin is often not physical, as uncertainties often correlate across similar actuators and this thus leads to a lower estimation. Overall, the results represent a highly conservative estimation of the closed-loop robustness and are limited to local (linear) effects, although dynamic maneuvers could be beneficial for the vehicle's robustness.

Future work should focus on experimental flight testing and validation, as well as extending the robustness analysis to other methods, such as nonlinear anti-optimization, an integrated robustness metric, or LPV/LTV systems.

## Appendix

**Table 4 Weight and balance parameter values**

Symbol	Description	Value
$m_f$	Fuselage mass	585.8 kg
$m_{w1}$	Main wing mass	103.7 kg
$m_{w2}$	Canard wing mass	90.5 kg
$J_{f,cm}^B$	inertia of fuselage	$\begin{bmatrix} 157.44 & 0 & -34.16 \\ 0 & 987.62 & 0 \\ -34.16 & 0 & 911.99 \end{bmatrix}$ kg m <sup>2</sup>
$J_{w1,cm}^{W1}$	inertia of rear wing	$\begin{bmatrix} 448.45 & 0 & -74.93 \\ 0 & 214.41 & 0 \\ -74.93 & 0 & 590.65 \end{bmatrix}$ kg m <sup>2</sup>
$J_{w2,cm}^{W2}$	inertia of front wing	$\begin{bmatrix} 350.54 & 0 & -113.01 \\ 0 & 565.48 & 0 \\ -113.01 & 0 & 865.62 \end{bmatrix}$ kg m <sup>2</sup>
$r_{f,cm}^B$	center of mass of fuselage	$[-2.94 \ 0 \ -1.35]$ m
$r_{w1}^B$	Hinge position of rear wing	$[-4.1533 \ 0 \ -1.94]$ m
$r_{w1}^B$	Hinge position of front wing	$[-0.4912 \ 0 \ -0.862]$ m
$r_{w1,cm}^{W1}$	center of mass of rear wing w.r.t. hinge	$[0.0781 \ 0 \ 0]$ m
$r_{w2,cm}^{W2}$	center of mass of front wing w.r.t. hinge	$[0.1279 \ 0 \ 0]$ m

**Table 5 Propulsion coefficients (cf. [38])**

Symbol	Description	Value
$c_{T_0}$	thrust coefficient	0.0258
$c_{T_\lambda}$		0.2373
$c_{Q_0}$	torque coefficient	0.00155
$c_{Q_\lambda}$		-0.0672
$c_{H_\lambda}$	H-force (or propeller drag) coefficient	0.05
$c_{P_\lambda}$	symm. propeller pitch moment coefficient	0.0174

## References

- [1] Bacchini, A., and Cestino, E., “Electric VTOL Configurations Comparison,” *Aerospace*, Vol. 6, No. 3, 2019. <https://doi.org/10.3390/aerospace6030026>.
- [2] Cook, J., “A Strip Theory Approach to Dynamic Modeling of eVTOL Aircraft,” *AIAA SCITECH 2021 Forum*, 2021. <https://doi.org/10.2514/6.2021-1720>, AIAA Paper 2021-1720.
- [3] Simmons, B. M., and Murphy, P. C., “Aero-Propulsive Modeling for Tilt-Wing, Distributed Propulsion Aircraft Using Wind Tunnel Data,” *Journal of Aircraft*, Vol. 59, No. 5, 2022, pp. 1162–1178. <https://doi.org/10.2514/1.C036351>.
- [4] May, M., Milz, D., Armanini, S., and Looye, G., “Transition Strategies for Tilt-Wing Aircraft,” *Journal of Guidance, Control, and Dynamics*, Vol. 48, No. 10, 2025, pp. 2326–2337. <https://doi.org/10.2514/1.G008257>.
- [5] Sullivan, T., “The Canadair CL-84 tilt wing design,” *Aircraft Design, Systems, and Operations Meeting*, 1993. <https://doi.org/10.2514/6.1993-3939>.
- [6] Droandi, G., Syal, M., and Bower, G., “Tiltwing Multi-Rotor Aerodynamic Modeling in Hover, Transition and Cruise Flight Conditions,” *AHS International 74th Annual Forum & Technology*, 2018.
- [7] North, D. D., Busan, R. C., and Howland, G., “Design and Fabrication of the LA-8 Distributed Electric Propulsion VTOL Testbed,” *AIAA SCITECH 2021 Forum*, 2021. <https://doi.org/10.2514/6.2021-1188>, AIAA Paper 2021-1188.
- [8] Panish, L., Nicholls, C., and Bacic, M., “Nonlinear Dynamic Inversion Flight Control of a Tiltwing VTOL Aircraft,” *AIAA SCITECH 2023 Forum*, AIAA, 2023. <https://doi.org/10.2514/6.2023-1910>, AIAA Paper 2023-1910.
- [9] Holsten, J., Ostermann, T., Dobrev, Y., and Moormann, D., “Model validation of a tiltwing UAV in transition phase applying windtunnel investigations,” *Congress of the International Council of the Aeronautical Sciences*, Vol. 28, International Council of the Aeronautical Sciences Bonn, Germany, 2012.
- [10] Cetinsoy, E., Dikyar, S., Hancer, C., Oner, K. T., Sirimoglu, E., Unel, M., and Aksit, M. F., “Design and construction of a novel quad tilt-wing UAV,” *Mechatronics*, Vol. 22, No. 6, 2012, pp. 723–745. <https://doi.org/10.1016/j.mechatronics.2012.03.003>.
- [11] Liu, Z., He, Y., Yang, L., and Han, J., “Control techniques of tilt rotor unmanned aerial vehicle systems: A review,” *Chinese Journal of Aeronautics*, Vol. 30, No. 1, 2017, pp. 135–148. <https://doi.org/10.1016/j.cja.2016.11.001>.
- [12] Hartmann, P., Meyer, C., and Moormann, D., “Unified Velocity Control and Flight State Transition of Unmanned Tilt-Wing Aircraft,” *Journal of Guidance, Control, and Dynamics*, Vol. 40, No. 6, 2017, pp. 1348–1359. <https://doi.org/10.2514/1.g002168>.
- [13] Dickeson, J. J., Miles, D., Cifdaloz, O., Wells, V. L., and Rodriguez, A. A., “Robust LPV  $H_\infty$  gain-scheduled hover-to-cruise conversion for a tilt-wing rotorcraft in the presence of CG variations,” *2007 46th IEEE Conference on Decision and Control*, IEEE, 2007. <https://doi.org/10.1109/cdc.2007.4435028>.
- [14] Cook, J., and Gregory, I., “A Robust Uniform Control Approach for VTOL Aircraft,” *Vertical Flight Society – 2021 Autonomous VTOL Technical Meeting and Electric VTOL Symposium*, 2021.
- [15] Daud Filho, A., and Belo, E., “A tilt-wing VTOL UAV configuration: Flight dynamics modelling and transition control simulation,” *The Aeronautical Journal*, Vol. 128, No. 1319, 2023, pp. 152–177. <https://doi.org/10.1017/aer.2023.34>.
- [16] Sobiesiak, L. A., Fortier-Topping, H., Beaudette, D., Bolduc-Teasdale, F., Lafontaine, J. D., Nagaty, A., Neveu, D., and Rancourt, D., “Modelling and Control of Transition Flight of an eVTOL Tandem Tilt-Wing Aircraft,” *8th European Conference for Aeronautics and Aerospace Sciences (EUCASS)*, Proceedings of the 8th European Conference for Aeronautics and Space Sciences. Madrid, Spain, 1-4 July 2019, 2019. <https://doi.org/10.13009/EUCASS2019-137>.
- [17] Autenrieb, J., Shin, H.-S., and Bacic, M., “Development of a Neural Network-based Adaptive Nonlinear Dynamic Inversion Controller for a Tilt-wing VTOL Aircraft,” *2019 Workshop on Research, Education and Development of Unmanned Aerial Systems (RED UAS)*, 2019. <https://doi.org/10.1109/REDUAS47371.2019.8999700>.
- [18] Axten, R. M., Khamvilai, T., and Johnson, E. N., “VTOL Freewing Design and Adaptive Controller Development,” *AIAA SCITECH 2023 Forum*, 2023. <https://doi.org/10.2514/6.2023-0401>.
- [19] Surmann, D., and Myschik, S., “Gain Design of an INDI-based Controller for a Conceptual eVTOL in a Nonlinear Simulation Environment,” *AIAA SCITECH 2023 Forum*, 2023. <https://doi.org/10.2514/6.2023-1250>.
- [20] Di Francesco, G., and Mattei, M., “Modeling and Incremental Nonlinear Dynamic Inversion Control of a Novel Unmanned Tiltrotor,” *Journal of Aircraft*, Vol. 53, No. 1, 2016, pp. 73–86. <https://doi.org/10.2514/1.C033183>.

- [21] Raab, S. A., Zhang, J., Bhardwaj, P., and Holzapfel, F., "Proposal of a Unified Control Strategy for Vertical Take-off and Landing Transition Aircraft Configurations," *2018 Applied Aerodynamics Conference*, American Institute of Aeronautics and Astronautics, 2018. <https://doi.org/10.2514/6.2018-3478>.
- [22] Lombaerts, T., Kaneshige, J., Schuet, S., Aponso, B. L., Shish, K. H., and Hardy, G., "Dynamic Inversion based Full Envelope Flight Control for an eVTOL Vehicle using a Unified Framework," *AIAA SCITECH 2020 Forum*, 2020. <https://doi.org/10.2514/6.2020-1619>.
- [23] Binz, F., Islam, T., and Moormann, D., "Attitude control of tiltwing aircraft using a wing-fixed coordinate system and incremental nonlinear dynamic inversion," *International Journal of Micro Air Vehicles*, Vol. 11, 2019, p. 175682931986137. <https://doi.org/10.1177/1756829319861370>.
- [24] Liu, Z., Guo, J., Li, M., Tang, S., and Wang, X., "VTOL UAV Transition Maneuver Using Incremental Nonlinear Dynamic Inversion," *International Journal of Aerospace Engineering*, Vol. 2018, 2018, pp. 1–19. <https://doi.org/10.1155/2018/6315856>.
- [25] Milz, D., and Looye, G., "Tilt-Wing Control Design for a Unified Control Concept," *AIAA SCITECH 2022 Forum*, 2022. <https://doi.org/10.2514/6.2022-1084>.
- [26] Milz, D., May, M., and Looye, G., "Dynamic Inversion-Based Control Concept for Transformational Tilt-Wing eVTOLs," *AIAA SciTech 2024 Forum*, AIAA, 2024. <https://doi.org/10.2514/6.2024-1290>.
- [27] Milz, D., May, M., and Looye, G., "Tandem Tilt-Wing Control Law Design using Hybrid Nonlinear Dynamic Inversion," *Journal of Guidance, Control, and Dynamics*, 2025. To be published.
- [28] Kumtepe, Y., Pollack, T., and Kampen, E.-J. V., "Flight Control Law Design using Hybrid Incremental Nonlinear Dynamic Inversion," *AIAA SCITECH 2022 Forum*, American Institute of Aeronautics and Astronautics, 2022. <https://doi.org/10.2514/6.2022-1597>.
- [29] Jiali, Y., and Jihong, Z., "An angular acceleration estimation method based on the complementary filter theory," *2016 IEEE International Instrumentation and Measurement Technology Conference Proceedings*, 2016. <https://doi.org/10.1109/I2MTC.2016.7520548>.
- [30] Milz, D., May, M., and Looye, G., "Flight Testing Air Data Sensor Failure Handling with Hybrid Nonlinear Dynamic Inversion," *Proceedings of the 2024 CEAS EuroGNC conference*, 2024.
- [31] Seiler, P. J., Packard, A., and Gahinet, P., "An Introduction to Disk Margins," *IEEE Control Systems*, Vol. 40, 2020, pp. 78–95. <https://doi.org/10.1109/MCS.2020.3005277>.
- [32] Pei, J., and Newsom, J., "Robust Stability Evaluation of the Space Launch System Control Design: A Singular Value Approach," *AIAA Atmospheric Flight Mechanics Conference*, 2015. <https://doi.org/10.2514/6.2015-1019>.
- [33] Simplício, P., Bennani, S., Marcos, A., Roux, C., and Lefort, X., "Structured Singular-Value Analysis of the Vega Launcher in Atmospheric Flight," *Journal of Guidance, Control, and Dynamics*, Vol. 39, No. 6, 2016, pp. 1342–1355. <https://doi.org/10.2514/1.G000335>.
- [34] May, M., Milz, D., and Looye, G., "Dynamic Modeling and Analysis of Tilt-Wing Electric Vertical Take-Off and Landing Vehicles," *AIAA SCITECH 2022 Forum*, 2022.
- [35] May, M. S., Milz, D., and Looye, G., "Semi-Empirical Aerodynamic Modeling Approach for Tandem Tilt-Wing eVTOL Control Design Applications," *AIAA SCITECH 2023 Forum*, 2023. <https://doi.org/10.2514/6.2023-1529>.
- [36] Ott, L., Milz, D., and May, M., "Design and Construction of a Modular 3D-Printed Tandem Tilt-Wing Testbed," *AIAA SCITECH 2026 Forum*, 2026.
- [37] May, M., Milz, D., Armanini, S. F., and Looye, G., "Impact of Failure on the Tilt-Wing eVTOL Backward Transition," *Journal of Aircraft*, Vol. 0, No. 0, 0, pp. 1–13. <https://doi.org/10.2514/1.C038391>.
- [38] May, M., Milz, D., and Armanini, S., "Transition Corridor Estimation for a Tilt-Wing Aircraft with Optimal Control-based Reachability Analysis," *AIAA SCITECH 2026 Forum*, 2026.
- [39] Sieberling, S., Chu, Q. P., and Mulder, J. A., "Robust Flight Control Using Incremental Nonlinear Dynamic Inversion and Angular Acceleration Prediction," *Journal of Guidance, Control, and Dynamics*, Vol. 33, No. 6, 2010, pp. 1732–1742. <https://doi.org/10.2514/1.49978>.

- [40] Wang, X., van Kampen, E.-J., Chu, Q., and Lu, P., “Stability Analysis for Incremental Nonlinear Dynamic Inversion Control,” *Journal of Guidance, Control, and Dynamics*, Vol. 42, No. 5, 2019, pp. 1116–1129. <https://doi.org/10.2514/1.g003791>.
- [41] Pollack, T., and Kampen, E.-J. V., “Multi-objective Design and Performance Analysis of Incremental Control Allocation-based Flight Control Laws,” *AIAA SCITECH 2023 Forum*, 2023. <https://doi.org/10.2514/6.2023-1249>.
- [42] Pfeifle, O., and Fichter, W., “Minimum Power Control Allocation for Incremental Control of Over-Actuated Transition Aircraft,” *Journal of Guidance, Control, and Dynamics*, Vol. 46, No. 2, 2023, pp. 286–300. <https://doi.org/10.2514/1.G006929>.
- [43] Joos, H.-D., Bals, J., Looye, G., Schnepper, K., and Varga, A., “A multi-objective optimisation-based software environment for control systems design,” *Proc. of CCA/CACSD 2002*, 2002.
- [44] Skogestad, S., and Postlethwaite, I., *Multivariable Feedback Control Analysis and Design*, John Wiley & Sons, 2001.
- [45] Holsten, J., Hartmann, P., and Moormann, D., “Modeling of Tiltwing Aircraft Dynamics as Linear System,” *6th EASN International Conference on Innovation in European Aeronautics Research, EASN2016*, 2016.